Studying Phonon Mean Free Paths
At the Nanoscale: Modeling and Experiments

by

Lingping Zeng

B.E. Department of Power Engineering, Huazhong University
of Science and Technology (2010)

S.M. Department of Mechanical Engineering, Massachusetts
Institute of Technology (2013)

Submitted to the Department of Mechanical Engineering
in partial fulfillment of the requirements for the degree of
Doctor of Philosophy in Mechanical Engineering

at the

MASSACHUSETTS INSTITUE OF TECHNOLOGY

September 2016

MASSACHUSETTS INSTITUTE
OF TECHNOLOGY
SEP 13 2016
LIBRARIES
ARCHIVES

© Massachusetts Institute of Technology 2016. All rights reserved.

Signature redacted

Author...

Department of Mechanical Engineering
August 19, 2016

Certified by .... Signature redacted

Gang Chen
Carl Richard Soderberg Professor of Power Engineering
Thesis Supervisor

Signature redacted

Accepted by ....

Rohan Abeyaratne
Chairman, Department Committee on Graduate Students

Studying Phonon Mean Free Path At the Nanoscale: Modeling and Experiments

by

Lingping Zeng

Submitted to the Department of Mechanical Engineering
on August 19, 2016, in partial fulfillment of the
requirements for the degree of
Doctor of Philosophy in Mechanical Engineering

Abstract

Heat conduction in semiconductors and dielectrics involves cumulative contributions from phonons with different frequencies and mean free paths (MFPs). Knowing the phonon MFP distribution allows us to gain insight into the fundamental microscopic transport physics and has important implications for many energy applications. The key metric that quantifies the relative contributions of different phonon MFPs to thermal conductivity is termed thermal conductivity accumulation function. In this thesis, we advance a thermal conductivity spectroscopy technique based upon experimental observation of non-diffusive thermal transport using wire grid linear polarizer in conjunction with time-domain thermoreflectance (TDTR) pump-and-probe measurement setup. Consistent algorithm based on solution from the phonon Boltzmann transport equation (BTE) is also developed to approximately extract the thermal conductivity accumulation functions in materials studied.

The heat flux suppression function appropriate for the experimental sample geometry relates the measured apparent thermal conductivities to the material's phonon MFP distributions. We develop a multi-dimensional thermal transport model based on the gray phonon BTE to find the suppression function relevant to our spectroscopy experiment. The simulation results reveal that the suppression function depends upon both the heater size and the heater array period. We also find that the suppression function depends significantly on the location of the temperature measurement. Residual suppression effect is observed for finite filling fractions (ratio of heater size to heater array period) due to the transport coupling in the underlying substrate induced by the neighboring heaters.

Prior phonon MFP spectroscopy techniques suffer from one or several of the following limitations: (1) diffraction limited to micrometer lengthscales by focusing optics, (2) applying only to transparent materials, or (3) involving complex micro-fabrications. We explore an alternate approach here using wire grid linear polarizer in combination with TDTR measurement. The wire grid polarizer is designed with sub-wavelength gaps between neighboring heaters to prevent direct photo-excitation in the substrate while simultaneously functioning as heaters and thermometers during the measurement. The spectroscopy technique is demonstrated in crystalline silicon by studying length-dependent thermal transport across a range of lengthscales and temperatures. We utilize the calculated heat flux suppression functions and the measured size-dependent effective thermal conductivities to reconstruct the phonon MFPs in silicon and achieve reasonably good agreement with calculation results from first principle density function theory.

Knowledge of phonon MFP distributions in thermoelectric materials will help design nanostructures to further reduce lattice thermal conductivity to achieve better thermoelectric performance in the next-generation thermoelectric devices. We apply the developed wire grid polarizer spectroscopy technique to study phonon MFP distributions in two thermoelectric materials: $Nb_{0.95}Ti_{0.05}FeSb$ and boron-doped nanocrystalline $Si_{80}Ge_{20}B$. We find that the dominant phonon MFPs that contribute to thermal conductivity in those two materials are in the a few tens to a few hundreds of nanometers. The measurement results also shed light on why nanostructuring is an effective approach to scattering phonons and improve the thermoelectric behavior.

Thesis Supervisor: Gang Chen
Title: Carl Richard Soderberg Professor of Power Engineering

Acknowledgement

The completion of this thesis would not be possible without the help and support from many people. I would like to gratefully thank them here.

First, I would like to thank my advisor and mentor, Professor Gang Chen. After I came to MIT, I had been working with Professor Gang Chen on non-diffusive thermal transport and it was an incredible experience. Gang's patient guidance and advice shaped me into a better researcher. His dedication to research sets an example for myself. Gang also constantly drove me beyond the point that I believed I could not reach. I would also like to thank my other thesis committee, Professor Nicolas Hadjiconstantinou and Professor Keith Nelson. My discussion with Nicolas always kept me with the state-of-the-art Monte Carlo techniques that played an important part of my research at MIT. I learned tremendously by discussing with Keith on phonon spectroscopy and was always impressed by his spirit towards research.

I would like to thank all the members of the NanoEngineering group for their help in solving my research problems. In particular, I would like to thank Dr. Maria Luckyanova, Dr. Kimberlee Collins, Dr. John Cuffe, Dr. Amy Marconnet, Mr. Samuel Huberman, Mr. Vazrik Chiloyan, Dr. Xiaopeng Huang, Mr. George Ni, and Dr. Jonathan Tong for their frequent help and encouragement in both my research and my life outside research. Their presence made my research life at MIT enjoyable.

All my PhD research was collaborative in nature and could not be completed without the collective efforts from many people. I would like to thank Dr. Alexei Maznev, a scientific mentor for me, for his tremendous amount of help in analyzing phonon spectroscopy experiments and simulations. His critique always helped improve the quality of my research work. I benefited a lot from discussions with Professor Yongjie Hu and would like to thank him for the valuable input on the phonon spectroscopy. Dr. Jean-Philippe Peraud offered me countless help on the phonon Monte Carlo simulations and I owe him a big thanks. I would also like to thank Professor Zhifeng Ren, Dr. Weishu Liu, Dr. Qian Zhang, Mr. Ran He and Dr. Dezhi Wang for providing thermoelectric samples for MFP measurement.

A big part of my research was to figure out the fabrication recipe for different samples. I could not remember how many times I talked to Kurt Broderick and Mark Mondol to ask them questions on lithography and liftoff. I would like to sincerely thank them for sharing so much of their time and thoughts with me. I would also like to acknowledge Mr. Xin Zhao and Mr. Wenjie Lu for their help on optimizing my fabrication recipe.

Many friends made my life outside research so enjoyable. I would like to thank Lei, Yu, Maria, John, Vazrik, Sam, George, Jonathan, David, Xiaopeng, Amy, Zhenlong, Leonardo, Yajun, Xiaoman, Linying, Grace, Diana, Jianjian, ..., for sharing your time with me. My life was full of colors with all of you guys! I would also like to thank my ballroom coaches Ben Moss, Fil Hsu and Esther for their tremendous help on my ballroom practices.

Finally, and above all else, I would like to thank my family for being constantly supportive for whatever career I chose, especially my father. Their ongoing support drives me to make the dreams in my life come true.

To my father!

Contents

1 Introduction **20**

1.1 Thermal Conductivity Accumulation Function 21

1.2 Phonon MFP Spectroscopy 23

1.3 Two-color Time-domain Thermoreflectance 29

1.4 Organization of this Thesis 36

2 Modeling Suppression Functions for Spectroscopy Experiments **39**

2.1 Simulation Details 40

2.2. Results and Discussion 47

2.3 Summary 56

3 Phonon MFP spectroscopy Using 1D Metallic Wire Grid Polarizer **58**

3.1 Structure Design and Optical Simulation 59

3.2 Sample microfabrication 62

3.3 Two-tint Time-domain Thermoreflectance 65

3.4 Heat Transfer Model for 1D Grating 67

3.5 Measurement Results and Discussion 68

3.6 MFP Reconstruction 75

3.7 Summary 82

4 Probing phonon MFP distributions in thermoelectrics **85**

4.1 Thermoelectrics Background 85

4.2 Sample preparation and pattern fabrication 87

4.3 Thermal conductivity measurement 91

4.4 MFP reconstruction and results discussion 96

4.5 Summary 98

5 Summary and Future Work **101**

5.1 Summary 101

5.2 Future Research 104

List of Figures

1-1 Thermal conductivity accumulation functions for a set of materials based upon first principle DFT calculations at room temperature [31]........................... 22

1-2 Schematic illustration of thermal transport regimes. (a) Heat transport is diffusive when heater size *w* is much larger than phonon MFPs. (b) Heat transport becomes quasiballistic when heater line width *w* is comparable to phonon MFPs... 25

1-3 Schematic diagram of the two-color TDTR setup in the Rohsenow Kendall Heat Transfer Laboratory at MIT.. 31

1-4 Schematic diagram of a multi-layer structure used in TDTR experiments........ 34

2-1 Sample structure. (a) Schematic diagram of the whole simulation domain; (b) representative of one period... 41

2-2 Finite differencing scheme used in the BTE. (a) Local phonon propagation direction, adapted from Ref. 4; (b) discretization schemes for different phonon propagation directions.. 43

2-3 Calculated interfacial thermal conductance as a function of time at different filling fractions when $w = 100$ nm.. 48

2-4 Demonstration of classical size effects by fitting the peak temperature rise. The results correspond to a heater width of 100 nm at a 10% filling fraction.......... 49

2-5 Effects of varying filling fractions w/L on k_{eff} by fitting the peak temperature rise. Open dots (squares, circles, and triangles) represent BTE results and solid lines represent the best fittings from Fourier's diffusion theory when the heater width is 100 nm. The corresponding effective thermal conductivities are 47.0 W/mK, 43.5 W/mK, and 37.5 W/mK for 83%, 50%, and 10% filling fractions, respectively, clearly showing the impact of filling fraction on the heat transport

in the underlying substrate... 50
2-6 Normalized effective thermal conductivities vs. normalized heater width at three different filling fractions by fitting the peak temperature rise............... 52
2-7 Effects of varying filling fractions on k_{eff} by fitting the peak-valley grating temperature difference. The data correspond to a heater width of 400 nm at three different filling fractions. Open dots (triangles, circles, and squares) are the BTE results and solid lines are the best fitting based on Fourier's law. The corresponding effective thermal conductivities for 10%, 50%, and 83% filling fractions are 47.2 W/mK, 43.0 W/mK, 30.0 W/mK, respectively, showing an opposite trend in the effective thermal conductivity while varying the filling fraction at the same heater width.. 54
2-8 Normalized effective thermal conductivities vs. normalized heater width at three different filling fractions by fitting the peak-valley grating temperature difference... 55

.

3-1 Optical simulation and transmittance measurement. (a) Schematic illustration of the optical simulation domain. (b) Simulated and measured transmittance of Al grating on sapphire versus the grating line width................................ 61
3-2 Schematic diagram of the transmittance measurement setup....................... 62
3-3 SEM image of a typical aluminum grating on silicon substrate.................... 64
3-4 AFM measurement of the metal thickness.. 64
3-5 Schematic diagram of the two-tint TDTR setup in Rohsenow Kendall Heat Transfer Laboratory at MIT.. 66
3-6 Measured silicon thermal conductivities (circles and squares), DFT computed thermal conductivity (diamonds), and the literature data (solid line, Ref. 103)... 69
3-7 Representative traces of measured room temperature TDTR reflectance signals (circles) and best model fits (solid lines) for three heater widths: 50 nm, 220

nm, and 2 μm. The effective thermal conductivities for these three samples are approximately 66.0 W/mK, 120.0 W/mK, and 140.0 W/mK, respectively........ 71
3-8 Silicon effective thermal conductivities versus heater width at 200 K, 250 K, 300 K and 350 K, respectively. The error bars represent standard deviations in the measured thermal conductivities. The filled dots represent silicon bulk thermal conductivity from literature (Ref. 104) at four different temperatures (circle: 200 K; square: 250 K; triangle: 300 K; diamond: 350 K)................. 72
3-9 Two-tint TDTR signal as a function of the angle between laser polarization and the metal grating lines for the 50 nm line width grating on silicon substrate...... 73
3-10 Two-color TDTR signal as a function of the angle between the laser polarization and the metal grating lines for the 50 nm wide grating on silicon substrate.. 74
3-11 Computed heat flux suppression functions at different filling fractions based on solving the phonon Boltzmann transport equation.................................... 78
3-12 Computed kernel functions versus filling fractions.................................. 79
3-13 Comparison of experimentally reconstructed silicon MFP distributions and predictions from DFT calculations at 200 K.. 80
3-14 Comparison of experimentally reconstructed silicon MFP distributions and predictions from DFT calculations at 250 K.. 80
3-15 Comparison of experimentally reconstructed silicon MFP distributions and predictions from DFT calculations at 300 K.. 81
3-16 Comparison of experimentally reconstructed silicon MFP distributions and predictions from DFT calculations at 350 K.. 81
4-1 SEM images of grain structures in (a) $Nb_{0.95}Ti_{0.05}FeSb$ and (b) $Si_{80}Ge_{20}B_{2.5}$, respectively. Figure (b) is adapted from Ref. 116.................................... 88
4-2 A representative AFM image of the surface roughness for a 10 um x 10 um area polished $Nb_{0.95}Ti_{0.05}FeSb$ area.. 90

4-3 A representative SEM image of the fabricated metal grating on the $Nb_{0.95}Ti_{0.05}FeSb$ substrate.. 91

4-4 Representative TDTR fits for the $Nb_{0.95}Ti_{0.05}FeSb$ substrate at three different heater sizes.. 92

4-5 Measured size-dependent $Nb_{0.95}Ti_{0.05}FeSb$ thermal conductivities across a range of temperatures. The filled dots represent the bulk thermal conductivities at the corresponding temperatures.. 92

4-6 Representative TDTR fits for the $Si_{80}Ge_{20}B_{2.5}$ substrate at three different heater sizes.. 95

4-7 Measured size-dependent $Si_{80}Ge_{20}B_{2.5}$ thermal conductivities at room temperature. The filled dot denotes the bulk thermal conductivity................ 95

4-8 Normalized size-dependent effective thermal conductivities of Si and $Si_{80}Ge_{20}B$ measured at room temperature.. 96

4-9 Reconstructed phonon MFP distributions for $Nb_{0.95}Ti_{0.05}FeSb$ at 200 K and 300 K. The dominant heat-carrying phonon MFPs are in the a few tens to a few hundreds of nanometers... 97

4-10 Reconstructed phonon MFP distribution for $Si_{80}Ge_{20}B_{2.5}$ at room temperature. The dominant thermal phonon MFPs are in the a few tens to a few hundreds of nanometers. The MFP spectrum comparison clearly shows that grain boundary scattering significantly suppresses the contribution of long-MFP phonons to thermal conductivity... 98

List of Tables

2.1 Material properties used in the phonon BTE calculation..41

3.1 Material optical properties at 785 nm (source: refractiveindex.info)....................62

Chapter 1

Introduction

Phonons are quantized lattice vibrations that transport heat and sound in solids. Heat conduction in non-metals generally involves dispersive lattice vibrations of variable frequencies and mean free paths (MFPs) [1]. The well-known heat diffusion theory relates the local heat flux to the local temperature gradient through the thermal conductivity in the diffusive transport regime where a local thermal equilibrium can be well defined. In the non-diffusive regime where the system characteristic lengthscale becomes comparable with or smaller than the phonon MFPs, however, defining local thermal equilibrium can be very challenging, and the Fourier's law breaks down due to a lack of phonon scattering events inherently assumed by the heat diffusion theory [2]–[5]. Studying non-diffusive thermal transport to determine phonon MFP distributions is currently of considerable interest [6]–[15]. Information on phonon MFPs provides insight into the fundamental physics of microscopic heat transport [16]–[21] and can guide material and device design for many technologies, such as thermal management of microelectronics [4], [5] and size effect engineering in thermoelectrics [22]–[31], to achieve better device performance. One important emerging research area, called phonon MFP spectroscopy [7]–[10], [12]–[15], [32]–[34], relies on the breakdown of the Fourier's law to determine which phonon MFPs contribute to thermal conductivity. This thesis explores the use of experimental observation of non-diffusive thermal transport in ultrafast optical spectroscopy and the solution of the Boltzmann transport equation (BTE) to approximately extract the phonon MFP distributions in a range of materials.

1.1 Thermal Conductivity Accumulation Function

Thermal transport in semiconductors and dielectrics is a broadband process that includes cumulative contributions from phonons with different frequencies and MFPs [35]–[39]. The phonon MFP describes the statistically average distance a phonon travels before scattering [1] and, under the relaxation time approximation, is given by: $\Lambda = V\tau$, where Λ, V, τ are the phonon MFP, group velocity, and phonon lifetime, respectively. One nice representation of a material's phonon MFP distribution is called the thermal conductivity accumulation function [40], defined as:

$$k_{accu}(\Lambda) = \frac{1}{3}\int_0^{\Lambda} CV\Lambda' \left(\frac{d\Lambda'}{d\omega}\right)^{-1} d\Lambda' \tag{1-1}$$

where C and ω are the mode dependent phonon specific heat and phonon radial frequency, respectively, and Λ' is a dummy variable. A summation over all the phonon branches is implied in Eq. (1-1). The thermal conductivity accumulation function represents the fractional thermal conductivity contribution from phonons with MFPs shorter than a threshold value Λ and essentially describes the distribution of phonon MFPs that contribute to a material's thermal conductivity.

The heat-carrying phonon MFPs in most materials of interest typically span several orders of magnitude from a few nanometers to a few tens of micrometers at room temperature [36], [38]. Figure 1-1, adapted from Ref. 31, shows the phonon MFP distributions from first-principles density function theory (DFT) calculations for several materials at room temperature [31]. As can be seen, different materials normally have different MFP spectra. For example, crystalline silicon has a broadly distributed MFP spectrum and approximately 50% of its thermal conductivity comes from phonon MFPs longer than 500 nm. In contrast, PbTe has a much narrower MFP distribution and most of its thermal conductivity is contributed by MFPs less than 100 nm. It is clear that heat-carrying phonons have a distribution of MFPs that cannot be accurately represented by any single value.

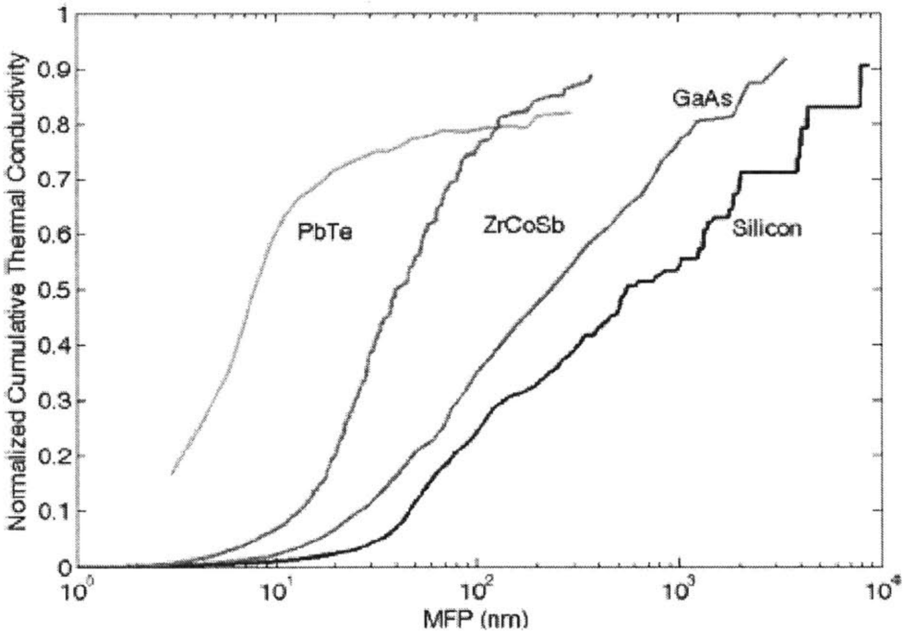

Figure 1-1. Thermal conductivity accumulation functions for a set of materials based upon first principle DFT calculations at room temperature [31].

In the old days, estimation of phonon MFPs relied on matching the model thermal conductivity built upon semi-empirical phonon lifetime models to experimentally measured thermal conductivity data [41], [42]. The predictions from these semi-empirical models are not accurate, though. At present, the thermal conductivity accumulation function can be directly computed from first-principles DFT based calculations without assuming any fitting parameter [36], [37], [39]. However, accurate DFT calculation is currently limited to simple single crystalline materials [43]. Computing MFP distributions in complex materials, such as nanocomposites and nanostructured thermoelectric materials, is still computationally prohibitive [44]. In principle, the MFP distribution can also be obtained directly from experimental measurements of phonon lifetimes and dispersion by inelastic neutron scattering [45], [46]. However, this requires measurements of phonon lifetimes across the entire Brillouin zone. Due to instrumental limitations of inelastic neutron scattering, this has been attempted so far only in a few materials with short phonon lifetimes. Moreover, inelastic neutron scattering is limited to characterizing single crystals and requires large-scale national facilities. This thesis investigates an alternate approach to determining a material's phonon MFP distribution indirectly from experimental observation of non-diffusive thermal transport at ultrashort lengthscales.

1.2 Phonon MFP Spectroscopy

The kinetic transport theory hints that a material's bulk thermal conductivity consists of contributions from all the heat-carrying phonon MFPs [40]. As a result, macroscopic property measurement in the diffusive transport regime probes the integral thermal conductivity contributed by all the phonon modes and therefore masks information about phonon MFP distribution [8], [47]. An emerging optical desk-top approach focuses on utilizing non-diffusive phonon transport, created when characteristic lengthscales become comparable to the phonon MFPs, to indirectly map out the MFP distributions [7]–[10], [13]. The idea is to measure transport across a characteristic length w, such that the contributions of phonons with MFPs larger than w to the thermal transport are suppressed. By varying w, information on relative contributions of phonons with different MFPs can be inferred. The characteristic length can be the size of the heat source [7], [8], [12], [13], the experimentally determined thermal transport distance [9], the thermal diffusion lengths traversed during an experimentally determined time period [6], [10], [11], or the dimension of a nanostructure [15]. Typically, this approach relies on the deviation of thermal transport from the Fourier law at small lengthscales [2]. In diffusive transport where the heat source dimension is much larger than the phonon MFPs, as shown in Fig. 1-2(a) for the experimental configuration to be used in the refined MFP spectroscopy study in this thesis, phonons undergo sufficient scattering to maintain local thermodynamic equilibrium and the heat conduction is accurately described by Fourier diffusion theory. In quasiballistic transport where the heat source dimension is comparable with some phonon MFPs, as shown in Fig. 1-2(b), long-MFP phonons do not experience scattering as inherently assumed by Fourier's law and no local thermal equilibrium can be established, leading to the breakdown of the heat diffusion theory [2]. Consequently, the measured thermal conductivity incorporates a quasiballistic thermal resistance that depends upon the characteristic thermal transport length in the measurement [2], [7], [8], [13]. By systematically varying the characteristic length to sample phonons of different MFPs and using a suppression function to connect the length-dependent thermal conductivity to MFPs, the phonon MFP distributions in the target materials can be extracted [48], [49].

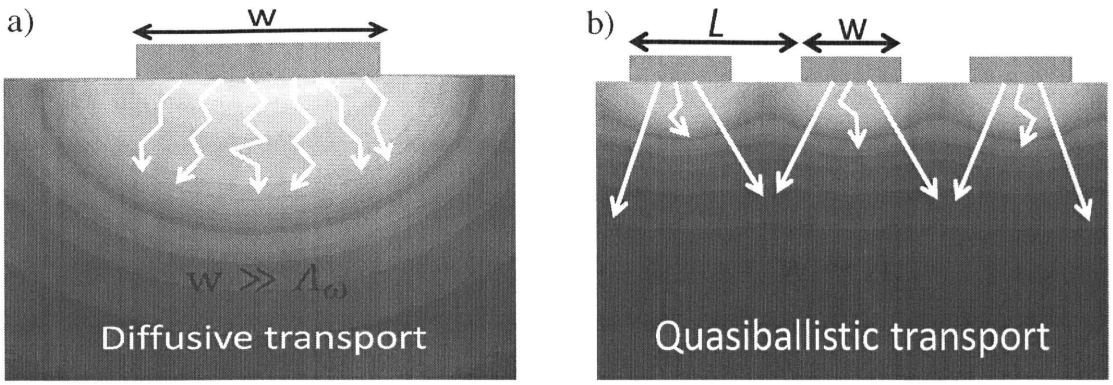

Figure 1-2. (a) Heat transport is diffusive when heater size *w* is much larger than phonon MFPs. (b) Heat transport becomes quasiballistic when heater line width *w* is comparable to phonon MFPs.

One nontrivial challenge to probe phonon MFPs is to reduce the characteristic lengthscale of the measurement such that quasiballistic transport can be sampled. In a laser-based experiment such as time-domain thermoreflectance (TDTR) [50], [51], the heater size can be readily varied by changing the heating laser spot size [8]. In particular, Minnich *et al.* [8] developed a pump-and-probe thermal conductivity spectroscopy technique to study phonon MFP distribution through measuring the effective thermal conductivities of silicon with different laser spot diameters. Significant non-diffusive thermal transport effect was observed at cryogenic temperatures where some phonon MFPs in silicon are much longer than the heating laser spot size. In a subsequent work performed with a transient thermal grating (TTG) setup, Johnson *et al.* [9] employed the interference of two pump laser beams to generate a sinusoidal transient grating temperature profile in a thin silicon membrane and another probe laser to measure the diffraction decay of this transient grating profile. Their measurements showed that the effective thermal conductivity of the membrane depends strongly on the grating spacing below 5 μm. The use of variable heating laser spot diameters in TDTR experiments or transient thermal grating periods in TTG experiments to access non-diffusive transport regime allows us to approximately measure the MFP distributions for a range of materials, but these approaches are ultimately diffraction-limited to characteristic thermal lengths around one micrometer for visible light beams.

To extend the diffraction-limited approaches to have nanometer spatial resolution such that materials with sub-micrometer phonon MFPs can be studied, micro-fabricated metallic grating nanostructures, either 1D metallic lines or 2D metallic nanodots, must be used. For example, Siemens *et al.* [7] employed a nanometer sized metallic line array as the heat absorbers and a soft X-ray as the probe to measure the decay of the diffracted beam due to transient heating of the metallic heat absorbers. They observed significant ballistic heat conduction effect as reflected in an increase of the effective thermal boundary resistance between the metallic heat absorbers and the studied sapphire substrate.

For pump-and-probe measurements, the use of nanodots or nanolines works well with transparent materials such as sapphire. However, for opaque materials, the excitation laser light will be absorbed not only by the metal heaters but also by the underlying material itself, complicating the data analysis. Additionally, if the material is a semiconductor, photo-excited carriers will contribute to the measured pump-and-probe experimental signal, complicating the data analysis further. To resolve these issues, Hu *et al.* [13] used a bilayer hybrid nanostructure to protect the substrate from direct laser heating. The bilayer nanostructure consists of a square array of aluminum nanodots and a hybrid layer that itself comprises of a layer of silver film sitting on top of an underlying polymer layer. The aluminum nanodots serve as heat absorbers and temperature transducers. The silver metal absorbs strongly the incident laser light but does not reflect significantly, thus contributing little to the measured signal at the detector. The underlying polymer functions as an insulting material to prevent the absorbed heat in the silver layer to penetrate into the substrate, essentially eliminating direct substrate heating. The hybrid nanostructure approach was applied to probe the phonon MFP distributions in a few materials, including sapphire, silicon, $Si_{0.99}Ge_{0.01}$, GaAs, and GaN. However, the hybrid nanostructured heater approach suffers from micro-fabrication complexity. Measuring diffraction of an extreme UV probe [12], predominantly sensitive to the photo-thermally induced surface displacement, largely alleviates the problems associated with electronic excitation and moderate substrate heating.

Another nontrivial challenge is the mapping of experimentally measured effective thermal conductivities to the phonon MFP distribution in the material under study [48], [49]. To infer the MFP distributions, the analysis in early studies was done using simple models based mainly on physical intuition, such as cutting off the contributions of phonons with MFPs exceeding the characteristic thermal length. The need for a more quantitative approach based on the Boltzmann transport equation (BTE) has been well recognized. In 2012, Professor Minnich at California Institute of Technology proposed a heat flux suppression function to link the length-dependent thermal conductivities to the material's intrinsic thermal conductivity accumulation function [49], [52], [53]:

$$k(w) = \int_0^\infty f(\Lambda)S(\eta)d\Lambda = \int_0^\infty F(\Lambda)K(\eta)\frac{d\eta}{d\Lambda}d\Lambda \tag{1-2}$$

where $\eta = \frac{\Lambda}{w}$ is the ratio of the phonon MFP to the characteristic thermal length, $k(w)$ is the length-dependent thermal conductivity, $f(\Lambda)$ is the differential thermal conductivity distribution function, $F(\Lambda)$ is the cumulative thermal conductivity distribution function (i.e. $k_{accu}(\Lambda)$), $S(\eta)$ is the heat flux suppression function, $K(\eta) = -dS/d\eta$ is kernel function. The cumulative thermal conductivity distribution function is related to the differential thermal conductivity distribution function through: $F(\Lambda) = \int_0^\Lambda f(\Lambda')d\Lambda'$. The suppression function represents the reduction in phonon heat flux from different MFP phonon modes for a given material system with respect to Fourier's law prediction. The key assumption is that the suppression function depends only upon the experimental configuration (i.e. the sample structure and the distribution of the heat sources), while the dependence of the measurement on the material properties is entirely described by the MFP distribution. This assumption enables extracting the MFP distribution from the measurement results without any prior knowledge of the phonon properties of the sample material. In addition, under that assumption, the same suppression function applies to a model "gray-body" medium in which all phonons have the same MFP. Thus the suppression function can be calculated from the gray-body phonon BTE. In reality, the above assumption is not entirely accurate and the suppression function in its rigorous form does depend upon material properties such as specific heat and phonon lifetime. However, it has been shown to work well, in comparison to the accurate spectral BTE solution, in describing thermal transport induced by a spatially periodic heat source [54] and thermal transport across and along thin films [15], [55].

Although the framework is built, such an approach has not yet been consistently implemented for extracting the MFP distribution from non-diffusive thermal transport measurements. One exception to the above statement is Ref. 15 where thermal transport in thin silicon membranes was measured in the diffusive regime across a range of membrane thicknesses and the well-established Fuchs-Sondheimer model was used to reconstruct the thermal conductivity accumulation function. However, the approach of Ref. 15 requires the fabrication of membranes spanning a broad range of thicknesses commensurate with the phonon MFPs, making it impractical as a generic MFP spectroscopy tool. In the hybrid nanodots approach mentioned before, Hu *et al.* [13] used single crystalline silicon as a benchmark material to solve the multidimensional suppression function by leveraging the measured size-dependent thermal conductivities and the known differential thermal conductivity distribution function from first principle DFT calculations. The reconstructed suppression function was subsequently utilized to extract the heat-carrying phonon MFP distributions in other studied samples.

1.3 Two-color Time-domain Thermoreflectance

The majority of the experimental work in this thesis is done using the TDTR setup in the Rohsenow Kendall Heat Transfer Laboratory in the mechanical engineering department at MIT. In this section, we give a brief overview of the principle of thermal conductivity measurement using TDTR [56]–[58].

As a non-contact and non-invasive pump-and-probe measurement technique, TDTR is uniquely suited to the property measurement of layered structures, including thin films, superlattices, and also bulk materials [50], [51], [59]. Typically, the sample is coated with a thin layer of metal film that serves as both heat absorber and temperature transducer. During the measurement, a periodic laser pulse called 'pump' impinges on the transducer surface, and is partially reflected and partially absorbed by a subset of free electrons in the metal. The temperature of the excited electrons may reach several thousand degrees Kelvin over the duration of one laser pulse due to the relatively small electronic heat capacity [60]–[63]. The excited electrons then quickly thermalize through electron-electron scattering within a few hundreds of femtoseconds [64]–[66]. The thermalized electrons interact with the metal lattice through scattering events to rapidly transfer the absorbed energy to phonons [67]. This typically occurs over a few to a few tens of picoseconds due to the large energy difference between electrons and phonons. For non-conductive substrates, phonon-phonon interaction between the metal transducer and the substrate conducts the heat energy from the metal to the substrate. For conductive substrates, heat can also diffuse to the substrate through a second electron-electron interaction channel.

Following the pump heating, another time-delayed probe beam is used to monitor the state of the sample at variable delay times that are regulated by a mechanical delay line. The probe beam detects the change in the sample's reflectance that is resulted from the change in the sample's surface temperature caused by the pump heating. In the linear response regime, measuring the reflectance change is essentially equivalent to probing the temperature change. The unknown thermal properties of the sample, typically the substrate thermal conductivity and the interface conductance between the metal and the substrate, are then extracted by matching the measured temporal reflectance signal to a diffusion heat transfer model.

A schematic of our TDTR setup is shown in Fig. 1-3 [68]. We use a mode locked Ti:Sapp laser as the laser source that outputs infrared light pulses at 800 nm wavelength with a repetition rate of ~80 MHz and a duration time of ~150 fs. The infrared light passes through an optical isolator that helps prevent any possible reflected laser beam from destabilizing the Tsunami cavity. Then the laser light goes through a combination of a half waveplate and a polarizing beam splitter (PBS) that split the majority of the light into a pump arm and the rest to a probe arm. After the beam splitting, the pump beam is modulated by an analog electro optic modulator (EOM) to enable lock-in signal detection. The modulated pump beam is subsequently frequency doubled from 800 nm to 400 nm through a second harmonic generator (SHG) optic to become spectrally different and distinct from the probe beam to ease beam separation. A pair of telescope lenses is used to control the size of the pump beam on the sample surface. The blue light after the SHG passes through a 10x microscope telescope and is focused onto the sample surface.

Following the beam splitting, the probe beam goes through a 4x beam expander to help reduce the beam divergence that occurs when it passes through the mechanical delay line that dynamically regulates the delay time between pump and probe beams. The delay stage in our setup gives a maximum of ~7 ns delay time. The probe beam is then recompressed to its original size and passes through the same 10x microscope telescope that focuses the probe beam coaxially with the pump beam onto the sample surface.

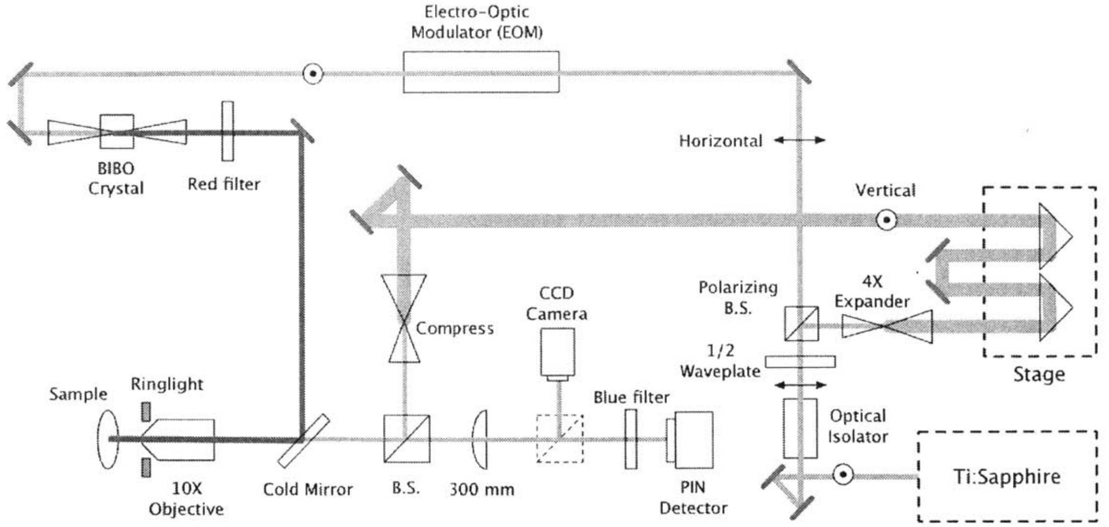
Electro-Optic
Modulator (EOM)
BIBO
Crystal
Red filter
Horizontal
Vertical
Compress
CCD
Camera
Polarizing
B.S.
4X
Expander
1/2
Waveplate
Stage
Sample
Ringlight
Blue filter
Optical
Isolator
Ti:Sapphire
10X
Objective
Cold Mirror
B.S.
300 mm
PIN
Detector

Figure 1-3. Schematic diagram of the two-color TDTR setup in the Rohsenow Kendall Heat Transfer Laboratory at MIT.

The complete overlap between pump and probe beams is important for the thermoreflectance measurement. To ensure an excellent overlap, we fix the position of the probe beam at the objective's focal plane and then adjust the position of pump beam to find the best overlap by maximizing the detected signal. To prevent any reflected pump beam from reaching the detector, we use a combination of a dichroic mirror and a blue filter in front the detector to allow only the reflected probe beam to enter the photodetector. The photocurrent is amplified by a trans-impedance amplifier and then passes through a low frequency band pass filter that is designed to only allow signal at the modulation frequency to be sent to the lock-in amplifier for detection. The lock-in amplifier mixes the input signal from the photodetector with a sinusoidal reference wave to generate the in-phase and quadrature components, i.e. X and Y, that are recorded by an automated LabView program. These two component signals are related to the sample's amplitude response, R, and phase response, ϕ, through the following formula:

$$R = \sqrt{X^2 + Y^2} \tag{1-3}$$

$$\phi = tan^{-1}(Y/X) \tag{1-4}$$

The amplitude R and phase ϕ, and the in-phase component X and quadrature component Y are related to the sample's thermal transfer function $Z(\omega_0)$ through:

$$Re^{i(\omega_0 t+\phi)} = Z(\omega_0)e^{i\omega_0 t} \tag{1-5}$$

$$Z(\omega_0) = X(\omega_0) + iY(\omega_0) \tag{1-6}$$

where ω_0 is the pump modulation frequency specified by a function generator that also sets the frequency of the sinusoidal reference wave in the lock-in amplifier. The thermal transfer function describes the sample's thermal response following periodic pump pulse heating and is typically obtained by solving the heat equation for a multi-layer structure. The thermal transfer function is given by [51]:

$$Z(\omega_0) = \frac{\beta Q Q_{probe}}{T^2} \sum_{k=-\infty}^{\infty} H(\omega_0 + k\omega_s)e^{ik\omega_s\tau} \tag{1-7}$$

where β is the thermoreflectance coefficient of the transducer film, Q and Q_{probe} are the absorbed pump and probe power, respectively, ω_s is the laser sampling frequency (80 MHz), T is the laser repetition period, τ is the delay time, and $H(\omega)$ is the sample's frequency response.

The frequency response $H(\omega)$ is typically derived from solving the multidimensional heat equation in the frequency domain for the layered sample structure. Figure 1-4 shows a representative sample structure with an index assigned to each layer from the top layer to the bottom layer. For the ith layer in the stack, we can relate the temperature and heat flux at the top of that layer to those quantities at the bottom of that layer through a transfer matrix [69]:

$$\begin{Bmatrix} \theta_{b,i} \\ f_{b,i} \end{Bmatrix} = \begin{Bmatrix} \cosh(qd) & -\frac{\sinh(qd)}{\sigma_z q} \\ -\sigma_z q \sinh(qd) & \cosh(qd) \end{Bmatrix} \begin{Bmatrix} \theta_{t,i} \\ f_{t,i} \end{Bmatrix} \tag{1-8}$$

where $q = \sqrt{\frac{\sigma_r k^2 + iC_v \omega}{\sigma_z}}$, σ_z is the cross-plane thermal conductivity, σ_r is the in-plane thermal conductivity, C_v is the volumetric heat capacity, ω is the periodic laser heating frequency, k is the Hankel transform variable, d is the layer thickness, and the subscripts b and t denote the bottom and top surfaces respectively. The transfer matrix equation (1-8) accounts for the anisotropic thermal conductivities. As shown in Eq. (1-8), each layer can be characterized by four independent parameters: cross-plane thermal conductivity, anisotropy, heat capacity, and the layer thickness.

For a stack of multiple layers, the transfer matrix can be derived by simply multiplying the transfer matrix for each layer:

$$M = M_n M_{n-1} \cdots M_2 M_1 \tag{1-9}$$

Material interface can be modeled by treating the interface as a layer with zero heat capacity and zero thickness. Considering energy conservation across an interface, the transfer matrix for a material interface is given by:

$$M = \begin{Bmatrix} 1 & G^{-1} \\ 0 & 1 \end{Bmatrix} \tag{1-10}$$

where G is the interfacial thermal conductance (inverse of interfacial thermal resistance) defined by the ratio of interfacial heat flux to the temperature difference across the interface [70].

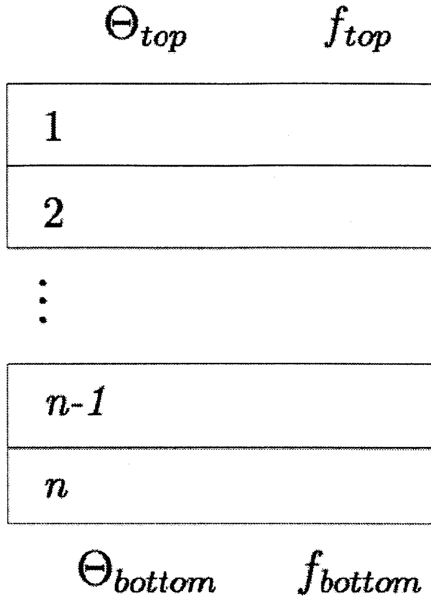

Figure 1-4. Schematic diagram of a multi-layer structure used in TDTR experiments (adapted from Ref. 68).

For a multi-layer sample structure, the temperature and heat flux at the bottom surface of the sample can be linked to the same quantities at the top surface of the sample through:

$$\begin{Bmatrix} \theta_b \\ f_b \end{Bmatrix} = \begin{Bmatrix} A & B \\ C & D \end{Bmatrix} \begin{Bmatrix} \theta_t \\ f_t \end{Bmatrix} \tag{1-11}$$

where the subscripts *b* and *t* denote the very bottom and top boundaries, and the matrix elements *A*, *B*, *C*, and *D* are determined by the material properties of each layer through the product of individual material matrices, as given in Eq. (1-9). To solve for the surface temperature, we need two boundary conditions, including the known heat fluxes at the bottom and top surfaces. At the bottom surface, the heat flux is zero since the substrate is typically a semi-infinite solid, leading to the following relation:

$$\theta_t = -\frac{D}{C} f_t \tag{1-12}$$

For pump heating with a Gaussian beam profile, the top surface heat flux in the Hankel transformed domain is given by:

$$f_t = \frac{A_0}{2\pi} \exp\left(-\frac{k^2 w_0^2}{8}\right) \quad (1\text{-}13)$$

where A_0 and w_0 are the absorbed pump power and pump beam diameter, respectively. After substituting Eq. (1-13) into the surface temperature Eq. (1-12) and weighting the surface temperature by a similar Gaussian profile of the probe beam with an $1/e^2$ radius of w_1, we can then perform an inverse Hankel transform to find the final frequency response of the sample:

$$H(\omega) = \frac{A_0}{2\pi} \int_0^\infty k\left(-\frac{D}{C}\right) \exp\left(-\frac{k^2 (w_0^2 + w_1^2)}{8}\right) dk \quad (1\text{-}14)$$

This frequency response function is substituted into Eq. (1-7) to model the heat transfer in the sample under periodic pulsed heating and a non-linear least square fitting algorithm is used to match the measured reflectance with the solution based on the diffusion heat transfer model to extract the unknown system properties.

We note that the above-presented model is valid in the diffusive transport regime. For this thesis's purpose to probe phonon MFP distributions, non-diffusive thermal transport must be studied. In the non-diffusive regime, we match the experimental signal with the diffusion model prediction with a modified thermal conductivity. In addition, to prevent carrier excitation in the substrate, we will discuss some key modifications made to the original two-color TDTR system in Chapter 3 to minimize the laser transmission through the microfabricated metal grating that is designed to access the non-diffusive regime [14], [71].

1.4 Organization of this Thesis

This thesis is a continued effort of the author's master thesis. In particular, this thesis completes the suppression function simulation initiated in the master thesis and extends the nanodots approach that was applied on a transparent sapphire crystal to studying heat carrier MFP distribution in opaque materials. The goal of this thesis is to develop a generic phonon MFP spectroscopy tool that can be applied to probe MFP distributions for both transparent and opaque samples. In addition, another goal is to develop a consistent approach based the phonon BTE to connect the experimentally measured thermal conductivities to the thermal conductivity accumulation functions in the materials studied. This thesis is organized as follows: the first chapter introduced some fundamental concepts about phonon MFP distribution, non-diffusive thermal transport, and described the current state-of-the-art techniques to either calculate or measure the MFP distribution.

In Chapter 2 we discuss the modeling of non-diffusive thermal transport in the experimental sample structure based on solving the multi-dimensional gray phonon BTE. We focus on the impact of different lengthscales on the heat flux suppression functions. The simulation results show that both the heater size and heater array period significantly affect the suppression function and transport coupling in the substrate induced by neighboring heaters leads to significant residual suppression for finite filling fractions. We also find that the effective thermal conductivity depends upon the location of the temperature measurement and care must be taken to correctly interpret the experimental results.

Chapter 3 presents the refined thermal conductivity spectroscopy technique using wire grid polarizers that function simultaneously as heat absorber and temperature transducer in the two-tint TDTR measurements. Both the sample structure and the measurement setup are designed to minimize laser transmission into the substrate, thus eliminating complex signal analysis from direct carrier excitation in the sample. We describe the modifications made to the original TDTR instrumentation to allow for sample heating at ~800 nm wavelength. Electromagnetic wave simulation using Comsol Multiphysics is carried out to show negligible light transmission through the grating structure. Experimental transmittance measurement and TDTR signal measurement by varying angles formed by metallic grating and laser polarization also suggest non-significant photo-excitation in the substrate. We demonstrate this approach by studying length dependent thermal transport in crystalline silicon across a range of temperatures and approximately extract the phonon MFP distributions using a convex optimization reconstruction algorithm based on the suppression function calculated in Chapter 2. We show that reconstructed MFP distributions agree reasonably well with first principle DFT calculations.

In Chapter 4 we discuss the application of the refined thermal conductivity spectroscopy technique to measure phonon MFP distributions in some select thermoelectrics. Detailed sample specific fabrication recipe is developed from the initial stage of polishing the sample surface to the final stage of patterning metallic gratings on top of the sample. We show that the dominant heat-carrying phonon MFPs in the materials studied are in the a few tens to a few hundreds of nanometers at room temperature and above. We also explore the impact of phonon-grain boundary scattering on the distribution of heat-carrying phonon MFPs in a nanocrystalline $Si_{80}Ge_{20}B$ sample. The measurement results show that introducing nano-sized grains significantly reduces the phonon MFPs that contribute to thermal transport.

Chapter 5 summarizes this thesis and describes some potential future work.

Chapter 2

Modeling Suppression Functions for Spectroscopy Experiments

Recent experimental observations of non-diffusive thermal transport have been utilized in thermal conductivity spectroscopy techniques to quantify the phonon MFP distributions in various materials of interests. Micro-fabricated grating nanostructures were used to extend the diffraction-limited approaches to probe materials with sub-micrometer heat-carrying phonon MFPs [7]–[9], [12]–[14]. We would like to note that transient grating experiments measure the temporal temperature difference between the peak and the valley of the grating period, either formed by metallic absorbers [7], [12]or by crossing two laser beams [9], [54], [72]–[74], while the TDTR approach measures the temporal temperature profile of the metallic heat absorbers [8], [13], [14].

In the non-diffusive transport regime, no local thermal equilibrium can be defined and thus the conventional heat diffusion theory breaks down [75]–[77]. To analyze the transport physics, the phonon BTE must instead be solved [2], [78]–[83]. In this Chapter, we develop a theoretical framework based upon the phonon BTE to model the suppression functions in the metallic line grating spectroscopy experiments [49], [84], [85]. We numerically study the impact of heater size and heaters' spacing on the thermal transport regime in the underlying substrate by solving multidimensional phonon BTE under transient heating conditions. We compute the peak temperature rise of the heaters that corresponds to the measured reflectance signal in the TDTR experiment [8], [13], [14] and is also of interests for microelectronics and nanowire/nanotube based thermal interface materials. The surface temperature difference between the peak and the valley of such periodic structures, corresponding to measurements in the diffraction-based experiments [7], [9], [12], is also calculated. Using these two temperatures as 'measured' signals, the effective thermal conductivities k_{eff} of the substrate that encode the degree of ballistic thermal transport are fit by matching the solution of the heat equation with that of the phonon BTE across a wide range of lengthscales. We find that both the heater size and the spacing between neighboring heaters have strong impact on the transport regime. The simulation results also show that the degree of ballistic thermal transport depends on what is measured: for the peak temperature rise, the ballistic effect diminishes as the heaters get closer, while for the peak-valley temperature difference, ballistic effect increases.

2.1 Simulation Details

In the non-diffusive regime, many phonons have MFPs longer than the characteristic thermal lengthscales and do not scatter in the locally heated region. Analyzing heat transfer in this regime requires solving the phonon BTE [86]–[90]. In this Chapter, we investigate the heat transport regime in the underlying substrate with periodic nanoscale line heaters on top under transient heating conditions. In general, the phonon BTE is difficult to solve since the phonon distribution function is a scalar in the six dimensional phase space. The simulation domain is sketched in Fig. 2-1(a). To make the computations tractable, the heater and substrate are modeled as materials with phonons being the heat carriers. The material properties, listed in Table 2.1, are chosen based on sensitivity consideration and assumed to be temperature independent. In addition, to compensate for the computational cost associated with solving the frequency dependent BTE, the developed transport model is based upon a gray two-dimensional phonon BTE [4], meaning that all the phonons in the heater and the substrate assume the same respective transport properties. Although existing studies all show that phonon MFP spans a wide range [36], [44], the constant MFP assumption helps to understand the physics and simulation results are useful for reconstructing phonon MFP distributions from experimental data through thermal conductivity suppression function [49].

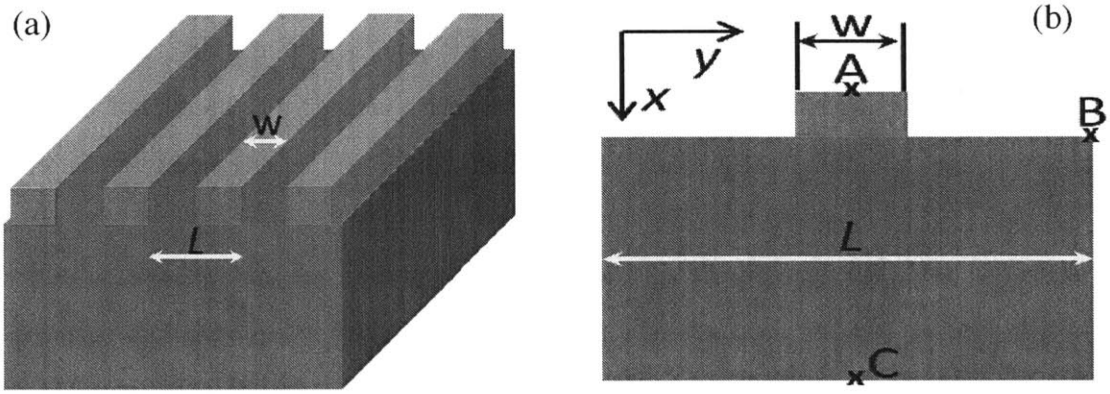

Figure 2-1. (a) Schematic diagram of the simulation domain; (b) representative of one period.

Table 2.1 Material properties of the heater and substrate.

Material	Bulk *k* (W/mK)	C_v (J/m^{3}K)	*V* (m/s)	Λ (nm)
Heater	100	2.35E6	3000	42
Substrate	50	1.0E6	1500	100

The transient phonon BTE under the relaxation time approximation is given by [75]:

$$\frac{\partial I}{\partial t} + \vec{V} \cdot \nabla I = -\frac{I - I_0}{\tau} \qquad (2\text{-}1)$$

where $I(x, y, \theta, \varphi, t) = \frac{1}{4\pi} \sum_p \int_0^{\omega_{m,p}} \hbar\omega f_\omega D_{\omega,p} V_{\omega,p} d\omega$ is the local directional phonon intensity along the propagation direction (θ, φ) (θ: polar angle, φ: azimuthal angle, as sketched in Fig. 2-2(a)), V is the phonon group velocity, τ is the gray phonon lifetime, and $I_0(x, y, t)$ is the equivalent equilibrium phonon intensity used to resolve the spatial and temporal temperature distribution. In the definition of the phonon intensity I, $\hbar\omega$ is the phonon quanta energy, f_ω is the spectral phonon occupation function, $D_{\omega,p}$ is the spectral density of phonon states for polarization p, $V_{\omega,p}$ is the spectral group velocity, and $\omega_{m,p}$ is the maximum vibration frequency for polarization p. The difficulty of solving Eq. (2-1) originates from obtaining I_0 since it averages the directional phonon intensity over the entire solid angle. The numerical technique has been thoroughly described elsewhere and is only briefly discussed here.

During the simulation, the discrete ordinate method is used to solve the phonon BTE together with a two-dimensional Gauss-Quadrature to integrate properties over the 4π solid angle [4]. An explicit first-order finite differencing method is implemented to perform both temporal and spatial derivatives in the phonon BTE. The initial temperature distributions inside the heaters and the substrate are assumed to be uniform, respectively, but differ by 1K. That temperature difference, small enough to justify the use of constant material properties, drives a heat current between them. The discretized BTE form depends upon the phonon propagation direction, as shown by the differencing schemes in Fig. 2-2(b), where $\mu = cos\theta$ is the directional cosine and η is defined as $\eta = sin\theta cos\varphi$. In general, backward differencing is taken when phonons travel along the positive direction, and vice versa. For example, assuming isotropic medium, the discretized BTE for the quadrant $\mu < 0, \eta > 0$ is given by:

$$\frac{I_{i,j,n,m}^{k+1}-I_{i,j,n,m}^{k}}{\Delta t}+V\mu\frac{I_{i+1,j,n,m}^{k}-I_{i,j,n,m}^{k}}{\Delta x}+V\eta\frac{I_{i,j,n,m}^{k}-I_{i,j-1,n,m}^{k}}{\Delta y}=-\frac{I_{i,j,n,m}^{k}-I_{i,j,0}^{k}}{\tau} \tag{2-2}$$

where i, j, n, m, and k are the x, y, μ, η, and time indices, respectively, $I_{i,j,n,m}^{k}$ is the phonon intensity at a specific point (i, j, n, m) in the phase space and time k, and $I_{i,j,0}^{k}$ is the equivalent equilibrium intensity at time k. Similarly, the discretized transport equation for other propagation directions can be written down. This explicit scheme is used to propagate in time until the expected simulation time is reached.

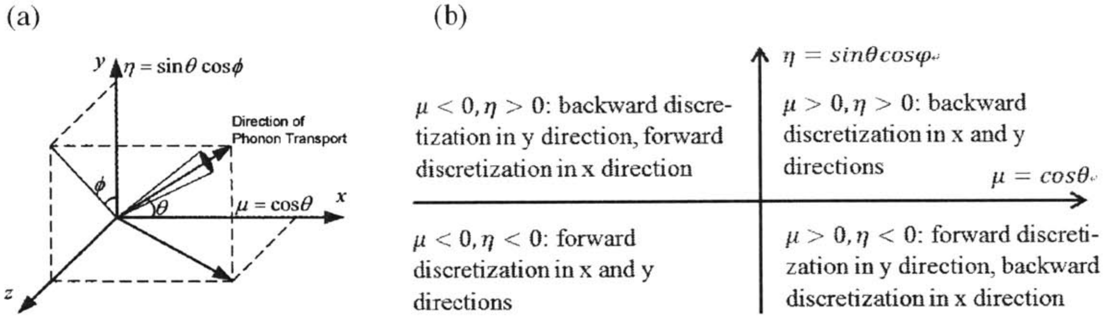
(a)
(b)
y
$\eta = \sin\theta\cos\phi$
Direction of Phonon Transport
ϕ
θ
$\mu = \cos\theta$
x
z
$\eta = sin\theta cos\varphi$
$\mu < 0, \eta > 0$: backward discretization in y direction, forward discretization in x direction
$\mu > 0, \eta > 0$: backward discretization in x and y directions
$\mu = cos\theta$
$\mu < 0, \eta < 0$: forward discretization in x and y directions
$\mu > 0, \eta < 0$: forward discretization in y direction, backward discretization in x direction

Figure 2-2. (a) Local phonon propagation direction, adapted from Ref. 4; (b) discretization schemes for different phonon propagation directions.

A two-dimensional Gaussian-Quadrature is implemented in the simulation to discretize the directional angles μ and φ. In particular, we discretize the directional cosine μ from -1 to 1 into $N_\mu = 40$ points and the azimuthal angle φ from 0 to π (not $0{\sim}2\pi$ due to symmetry) into $N_\varphi = 30$ points. The corresponding weights ω_n and ω_m^* for each propagation direction (μ, η) is computed through a numerical program and satisfy $\sum_{n=1}^{N_\mu}\sum_{m=1}^{N_\varphi}\omega_n\,\omega_m^* = 2\pi$. To guarantee stability and accuracy, the spatial and time steps must be sufficiently small and satisfy:

$$\Delta t < \frac{\Delta x_{min}}{V} \tag{2-3}$$

where Δx_{min} is the minimum spatial step size and V is the phonon group velocity. In this study, the spatial step size is chosen to be equal to or less than one twentieth of the smaller phonon MFP of the heater and the substrate, therefore ensuring stability and convergence.

Once initialized, the rate of heat rejection depends strongly upon the interfacial thermal properties, i.e. phonon transmittance and reflectance at the heater-substrate interface [70], [91]–[94]. Phonon scattering at the metal-substrate interface is assumed to be completely diffuse, which implies that phonons leaving the interface on either side of the interface bear an isotropic distribution [79]. Energy conservation requires the transmittance and reflectance to obey the following relation:

$$R + T = 1 \tag{2-4}$$

where R and T are the reflectance and transmittance on either side of the interface. At thermal equilibrium, the net heat flux across an interface is exactly zero, as required by the principle of detailed balance [1] which relates the transmittances on either side of an interface to one another by:

$$T_{21} = \frac{C_{V1}V_1}{C_{V2}V_2} T_{12} \tag{2-5}$$

where T_{12} is the transmittance from medium 1 to medium 2, T_{21} is the transmittance from medium 2 to medium 1, and C_{vi} and V_i (i=1, 2) are the volumetric specific heat capacities and speeds of sound, respectively. To obtain the transmittances, we first specify the transmittance T_{12} ($T_{12} = 0.1$). Then T_{21} can be straightforwardly determined through Eq. (2-5). When solving the diffusion heat transfer model, an interfacial thermal conductance G_{diff} is needed as the input and is determined from the phonon transmittances by [1], [80]:

$$G_{diff} = \frac{T_{12}C_{V1}V_1}{4(1-0.5(T_{12}+T_{21}))} \tag{2-6}$$

No size dependence of the interfacial thermal conductance is assumed, consistent with recent experiments [8]. Simulation results to be presented later will also validate this assumption.

The periodicity of the computed structure allows us to simulate one period of the structure, as shown in Fig. 2-1(b). The thicknesses of the heater array and the substrate are 80 nm and 3 μm respectively. In reality, the substrate is a semi-infinite system with its backside being adiabatic. In practice, by checking the substrate backside temperature rise, we find that 3 μm is sufficiently thick to approximate the substrate as a semi-infinite body. We also find that doubling the substrate thickness to 6 μm causes almost no difference in the peak temperature rise and peak-valley temperature difference. The left and right boundaries of the substrate in Fig. 2-1(b) are periodic boundaries [86]. We implement the periodic boundary condition as a specular reflection. All other free boundaries (including the free surfaces of the heater and the gaps between neighboring heaters) are modeled as being adiabatic. The effects of these free boundaries' specularity (fraction of phonons being specularly reflected) are checked by comparing the BTE results under totally specular and totally diffuse boundary conditions. Our simulation results show almost no specularity dependence from such comparison, thus we also model these free surfaces as specularly adiabatic walls.

The equivalent equilibrium phonon intensity [4], [80], corresponding to a locally thermalized equilibrium state, is computed by weighting all the directional intensities through:

$$I_0^k(x,y,t) = \frac{1}{2\pi}\sum_{n=1}^{N_\mu}\sum_{m=1}^{N_\varphi} I^k(x,y,\theta,\varphi,t)\omega_n\omega_m^* \qquad (2\text{-}7)$$

where $I^k(x,y,\theta,\varphi,t)$ is the directional phonon intensity at (x, y) along the direction (θ,φ) at time t. Instead of calculating the local thermodynamic equilibrium temperature which does not exist in highly non-equilibrium transport, we compute the equivalent equilibrium temperature [4], [80] that is a measure of the local energy density and defined as:

$$T(x,y,t) = \frac{4\pi}{CV} I_0^k(x,y,t) \tag{2-8}$$

The local heat flux along a specific direction consists of contributions from all the directional phonon intensities at the point being studied. For example, if we define the cross-plane direction as x, the local heat flux along this direction is given by:

$$q_x(x,y,t) = \frac{1}{2\pi} \sum_{n=1}^{N_\mu} \sum_{m=1}^{N_\varphi} I^k(x,y,\theta,\varphi,t) \mu_n \omega_n \omega_m^* \tag{2-9}$$

where μ_n is the directional cosine. Similarly, the heat flux along the in-plane direction can be written down as:

$$q_y(x,y,t) = \frac{1}{2\pi} \sum_{n=1}^{N_\mu} \sum_{m=1}^{N_\varphi} I^k(x,y,\theta,\varphi,t) \omega_n \omega_m^* \cos(\varphi_m) \tag{2-10}$$

where φ_m is the azimuthal angle.

The effects of heater dimension and spacing between neighboring heaters on the transport regime in the substrate of the proposed structure are studied under the framework of the developed thermal model. Heat transport occurs from the heaters to the underlying substrate after imposing an initial temperature difference between them. The presence of periodically arranged hot and cold spots in the computed structure generates thermal grating effects [9]. To gain insight into the heat conduction, we examine both the peak temperature rise (i.e. the temperature difference between points A and C, ΔT_{AC}, as indicated in Fig. 2-1(b)) and the temperature difference between the grating peak and valley (i.e. the temperature difference between points A and B, ΔT_{AB}, as indicated in Fig. 2-1(b)). The temporal decays of the peak temperature rise and the peak-valley grating temperature difference from the diffusion heat equation are matched with the corresponding results from the phonon BTE to find the effective thermal conductivities that are then used to analyze the heat transfer regime and derive the suppression functions for the grating geometry.

2.2. Results and Discussion

Two important length scales affecting the heat transfer are the heater width w and the period L (heater spacing = $L - w$) of the heater array. The simulations are carried out by varying the heater width w under different filling fractions (FF) defined as the ratio of the heater width to the heater array period w/L. This means that we systematically tune the heater width w while maintaining the filling fraction w/L at constant values to examine the effects of these two parameters on the thermal transport. Hereafter, without explicit explanation, we refer the phonon MFP or Λ to the substrate phonon mean free path.

As discussed before, we assumed that the interfacial thermal conductance has negligible size dependence. This assumption is validated from our simulation results, as shown in Fig. 2-3 that plots the calculated temporal interfacial thermal conductance G (based on the temporal interfacial heat flux and temperature difference across the interface) from the phonon BTE at different filling fractions when the heater width is 100 nm. Clearly, G increases with increasing filling fraction at a fixed heater width. However, the overall variation of G is within 6% and thus can be neglected. The computed interfacial thermal conductances for other geometries, including small and large heater widths relative to the phonon MFP, fall in the same range (2.50 $\sim$ 2.64 x 10^8 W/m^{2}K). In addition, we note that the magnitude of the calculated G is very close to the value G_{diff} predicted by Eq. (2-6): 2.465 x 10^8 W/m^{2}K. Consequently, we implement a constant interfacial thermal conductance computed from Eq. (2-6) when solving the diffusion heat equation for different geometries and only fit the substrate thermal conductivity.

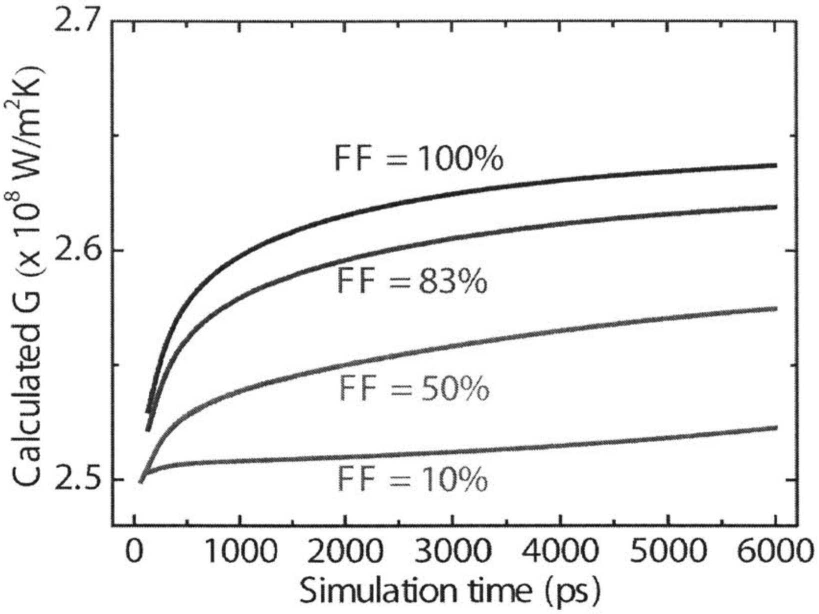

Figure 2-3. Calculated interfacial thermal conductance as a function of time at different filling fractions when w = 100 nm.

Figure 2-4 shows the decay of the peak temperature rise when the heater width is 100 nm (same as the substrate phonon MFP Λ) at a 10% filling fraction. The decay rate from the phonon BTE represented by the red squares is slower than that of Fourier's law represented by the green dashed curve obtained by using the bulk thermal conductivity of the substrate. The discrepancy between the diffusion result and the BTE data indicates the presence of ballistic transport in the substrate [84]. Our best fitting result returns an effective thermal conductivity $k_{\mathrm{eff}} \approx 37.5$ W/mK represented by the blue solid curve. This reduced substrate thermal conductivity implies that there is an additional ballistic resistance associated with transport in the substrate [7], [47].

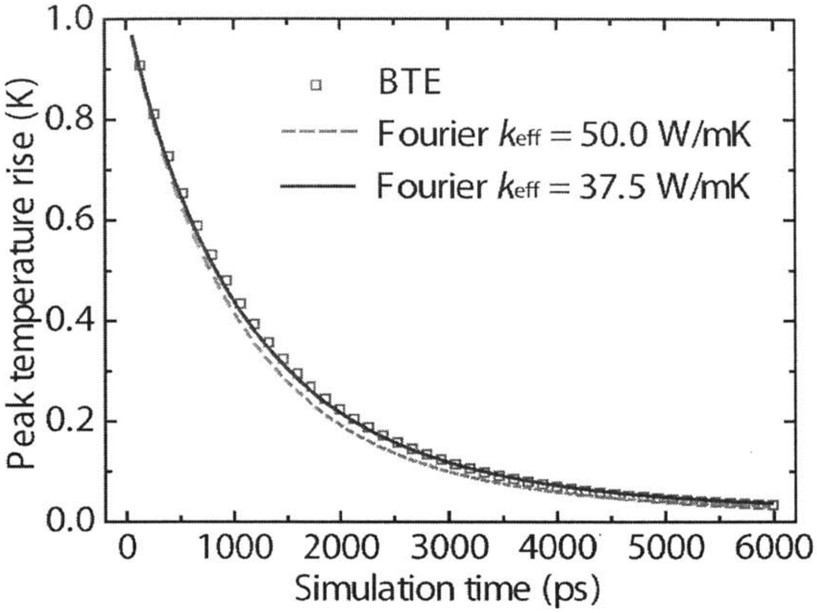

Figure 2-4. Demonstration of classical size effects by fitting the peak temperature rise. The results correspond to a heater width of 100 nm at a 10% filling fraction.

The effect of varying filling fractions is shown in Fig. 2-5 where the heater width is kept constant at 100 nm under three different filling fractions. The dots represent the data from the phonon BTE and the solid curves represent the best fittings from the diffusion heat equation. As the filling fraction increases from 10% to 83%, k_{eff} increases by approximately 20% from 37.5 W/mK to 47.0 W/mK, which indicates that the filling fraction, apart from the heater size, also significantly affects the thermal transport in the substrate. In the limit of zero spacing between heaters (100% filling fraction), the heater effectively becomes a continuous thin film covering the substrate and in this case our fitting returns the bulk thermal conductivity, consistent with prior pump-and-probe measurements.[8] Intuitively, for two structures with the same heater size, the structure with a larger filling fraction (smaller spacing) more closely approaches to the 'thin film heater case' and therefore has a higher k_{eff}. One can also view a continuous thin film heater as the superposition of many closely spaced point heat sources, and our results demonstrate that this superposition of closely spaced ballistic heat sources with identical heat generation actually leads to the familiar diffusive transport picture. This observation is important for designing thermal conductivity spectroscopy technique and also has many implications for thermal management of micro-/nanoelectronics and thermal interface materials. In microelectronics, heat may also be generated in a region of the MOSFET much smaller than the MFP of the substrate that spreads out the heat. Our calculation results suggest that the collective behavior caused by closely packed MOSFETs will reduce the ballistic effects present in an isolated nanoscale hot spot [4], [5]. Similarly, the predicted ballistic contact effect of an isolated point contact such as between a carbon nanotube and the underlying substrate may diminish in closely arranged carbon nanotube arrays used in thermal interface materials [95].

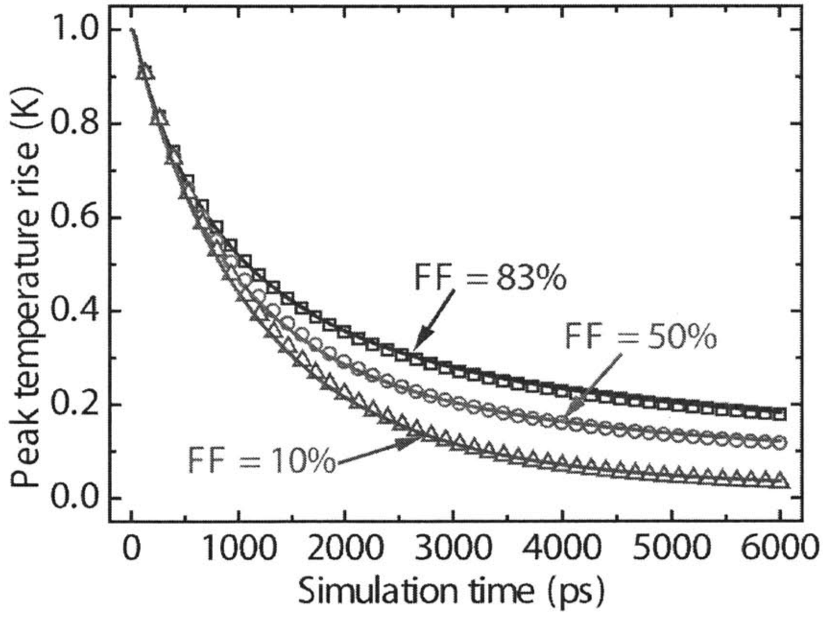

Figure 2-5. Effects of varying filling fractions w/L on k_{eff} by fitting the peak temperature rise. Open dots (squares, circles, and triangles) represent BTE results and solid lines represent the best fittings from Fourier's diffusion theory when the heater width is 100 nm. The corresponding effective thermal conductivities are 47.0 W/mK, 43.5 W/mK, and 37.5 W/mK for 83%, 50%, and 10% filling fractions, respectively, clearly showing the impact of filling fraction on the heat transport in the underlying substrate.

Figure 2-6 further shows the normalized effective substrate thermal conductivities (i.e. the suppression functions $S\left(\frac{w}{\Lambda}, FF\right) = \frac{k_{eff}(\frac{w}{\Lambda}, FF)}{k_{bulk}}$) as a function of the normalized heater width w/Λ at three different filling fractions. When the heater width w is appreciably larger than the phonon MFP ($w/\Lambda \approx 10$), phonons experience sufficient scattering to establish local thermal equilibrium and thus diffusive transport occurs in the substrate [11], [47]. In this scenario, the fitting returns the bulk thermal conductivity regardless of the filling fraction, as shown by Fig. 2-6. As the heater width is gradually reduced to a level comparable to the phonon MFP, some phonons travel ballistically and do not relax [47], [81]. Those ballistic phonons result in an additional ballistic thermal resistance that suppresses the rate of heat rejection through the conduction in the substrate, leading to a lower effective thermal conductivity. However, the degree of ballistic transport in the substrate under those three different filling fractions differs significantly as the heater width becomes comparable or small than the phonon MFP, as indicated by the substantially distinct effective thermal conductivities. For the very large filling fraction, represented by the blue curve, the transport is more diffusive compared with the transport at those two smaller filling fractions, which again implies that the collective behavior due to the interaction between closely spaced nanoscale heat sources significantly diminishes the non-diffusive transport effect that occurs in the case of an isolated nanoscale heat source. We also note that heat generation in current MOSFETs is typically confined to be around a tiny small region (much smaller than the gate length) near the drain side, thus the predicted impact of collective behavior may not reduce the non-local effects substantially due to the small filling fraction. However, as the gate length continues to shrink, we expect such collective behavior to have significant influence in reducing the degree of non-local transport.

As discussed before, periodically arranged nanoscale heat sources are required in the pump-and-probe techniques to probe short phonon MFP materials [47]. Typically, a set of effective thermal conductivities is measured with respect to some characteristic thermal lengthscales, i.e. heater sizes. Phonon MFPs are subsequently estimated by assuming the heat transfer suppression of phonons with MFPs exceeding the heater dimension [8], [47]. Our simulation results indicate that accurate interpretation of the measured effective thermal conductivities and phonon MFP reconstruction must take into account the impact of both the heater size and the spacing between neighboring heaters. In fact, as shown by Fig. 2-6, significant residual suppression occurs for finite filling fractions, meaning that the suppression function does not drop to zero even if when the ratio of phonon MFP to the heater size approaches zero. In contrast to an isolated heater, this happens due to the transport coupling in the substrate induced by the presence of the periodic heaters.

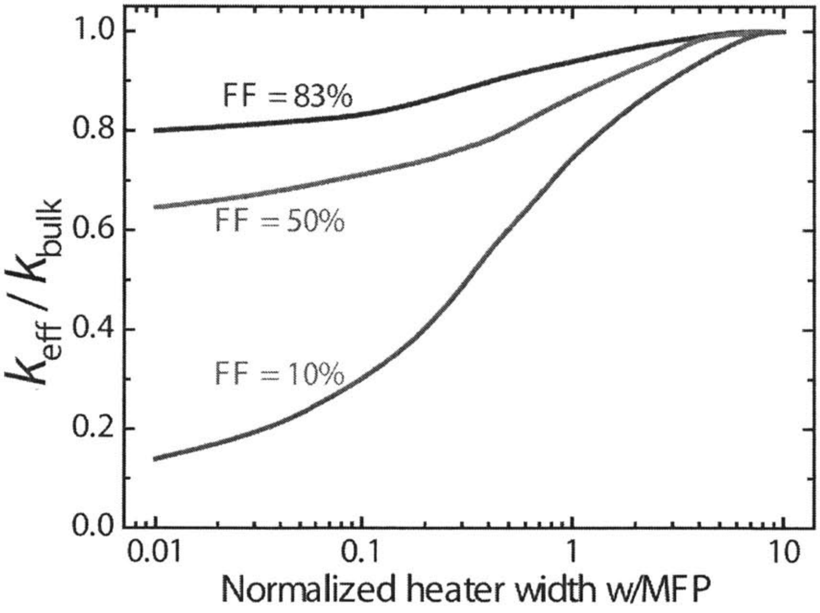

Figure 2-6. Normalized effective thermal conductivities vs. normalized heater width at three different filling fractions by fitting the peak temperature rise.

Interestingly, the effective thermal conductivities obtained via fitting the peak-valley temperature difference are inversely correlated to the filling fraction as opposed to fitting the peak temperature rise. Figure 2-7 shows the peak-valley temperature difference solutions from the phonon BTE together with the best fittings from the Fourier's diffusion theory for 400nm-sized heaters at three different filling fractions. Non-diffusive transport occurs for all three of these structures as can be seen from the obtained effective thermal conductivities. However, the structure with the largest filling fraction has the lowest thermal conductivity compared with other two cases. Physically this originates from the fact that the peak-valley temperature difference always measures the thermal transport between the two heaters as the valley is the lowest temperature point on the substrate surface [9]. The spacing between adjacent heaters becomes the characteristic thermal length while fitting the peak-valley temperature difference. For a fixed heater width, the structure with a larger filling fraction has a smaller spacing between adjacent heaters, consequently giving a lower effective thermal conductivity. The contradicting trends in the effective thermal conductivities obtained using the peak temperature rise of the heater and the temperature difference between the peak and the valley in a grating structure imply that a single effective thermal conductivity cannot perfectly match the results from the phonon BTE and the diffusion theory in the whole simulation domain [96]. Equivalently, the peak temperature rise and peak-valley temperature difference are associated with two different thermal lengths for the same structure and care must be taken when comparing the thermal conductivities measured by these two signals.

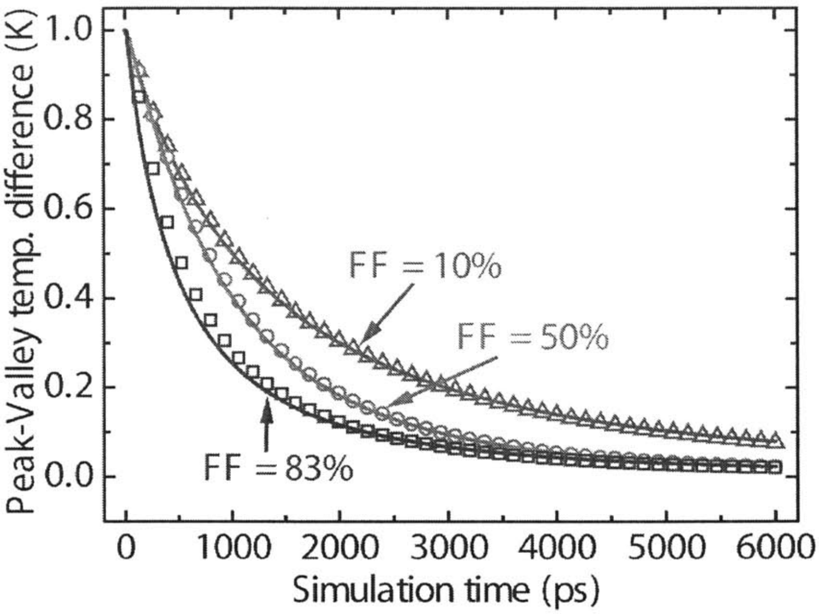

Figure 2-7. Effects of varying filling fractions on k_{eff} by fitting the peak-valley grating temperature difference. The data correspond to a heater width of 400 nm at three different filling fractions. Open dots (triangles, circles, and squares) are the BTE results and solid lines are the best fitting based on Fourier's law. The corresponding effective thermal conductivities for 10%, 50%, and 83% filling fractions are 47.2 W/mK, 43.0 W/mK, 30.0 W/mK, respectively, showing an opposite trend in the effective thermal conductivity while varying the filling fraction at the same heater width.

The thermal conductivities measured by the peak-valley temperature difference as a function of the normalized heater width is shown in Fig. 2-8. It is worth noting that for a large filling fraction, the k_{eff} is significantly lower than the bulk value even at a very large heater size ($w/\Lambda = 10$). This occurs because the spacing between heaters is still comparable to the phonon MFP despite of the large heater size.

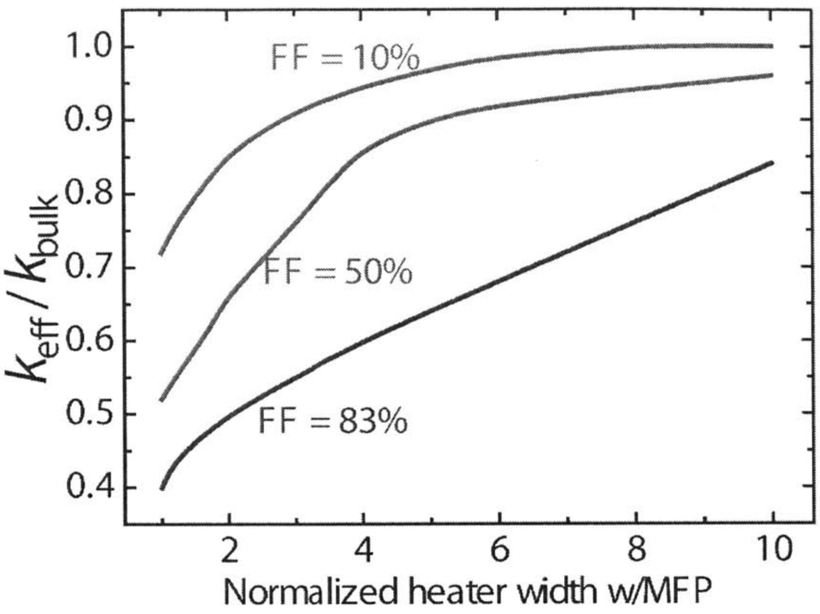

Figure 2-8. Normalized effective thermal conductivities vs. normalized heater width at three different filling fractions by fitting the peak-valley grating temperature difference.

Note that a single spectrum-averaged phonon MFP is used in this study to make the calculations tractable. In reality, phonon MFP in many materials varies by several orders of magnitude [10], [97]. Consequently, when the heater width or spacing between neighboring heaters falls within the range of the phonon MFP spectrum, long-MFP phonons travel ballistically and short-MFP phonons propagate diffusely, resulting in a much more complicated transport picture. Incorporating real phonon dispersion and frequency dependent MFPs makes a deterministic approach (for example, discrete ordinate method) to solving the phonon BTE expensive. More sophisticated technique, such as Monte Carlo method [87], [89], needs using to assess the effect of nonlinear phonon spectrum. Future work should focus on the implementation of newly developed variance-reduced Monte Carlo method to evaluate the impact of phonon dispersion on the thermal transport characteristics in the presence of periodical nanoscale heat sources.

2.3 Summary

We have studied the impact of heater size and heater spacing on the thermal transport regime in a substrate covered by periodic heat sources when either the heater width or the spacing becomes comparable to the phonon MFP. When the peak temperature rise and the peak-valley temperature difference are used as separate measures of the transport regime in the substrate, they give opposite trends in the substrate effective thermal conductivity as a function of the spacing between heaters. When only the heater temperature is of concern, we identified that the close spacing between neighboring heaters can reduce the ballistic transport effects which occur in the presence of an isolated nanoscale hot spot, consistent with the fact that in the limit that the heaters become a continuous film, both experimental and simulation results approach that of diffusive transport. On the other hand, if the peak-valley temperature difference on the surface is measured, ballistic effect becomes stronger as the spacing between heaters becomes smaller. These results are important for understanding experimental results in phonon MFP spectroscopy using TDTR method and transient thermal grating method, and for understanding the impact of scaling on the thermal management of micro- and nanoelectronics, and thermal interface materials. We will use the computed suppression functions to help extract the phonon MFP distributions in the wire grid polarizer spectroscopy experiments in the following two chapters.

Chapter 3

Phonon MFP spectroscopy Using 1D Metallic Wire Grid Polarizer

As discussed in Chapter 1, a generic phonon MFP spectroscopy technique would have sub-micrometer spatial resolution and apply to both transparent and opaque samples. To overcome these challenges, Hu *et al.* developed a hybrid nanodots approach [13] to effectively localizing the heating and preventing photo-excitation and direct substrate heating and demonstrated this approach by measuring phonon MFP distributions in a variety of materials. To simplify the microfabrication associated with this approach, we continue the efforts initiated by Dr. Kimberlee Collins, a previous graduate student in our laboratory, to refine the wire grid polarizer approach that is designed to probe the heat-carrying phonon MFPs in a generic sample [98]. In this Chapter, we discuss the progress made towards minimizing the photo-induced carrier excitation effect in the substrate observed in prior experimental efforts. The key feature of the wire grid polarizer approach is that the 1D array of metallic lines used as nanoscale heat absorbers is designed with subwavelength gaps between neighboring lines in order to simultaneously function as a wire grid polarizer, insulating the substrate from both photo-excitation and probe light, so that the standard TDTR measurement approach can be used without complications due to direct substrate heating and electron-hole generation. Compared with the EUV diffraction method [7], [12], this approach permits the measurement of thermal transport in similar nanostructured samples using more readily available optical probe wavelengths. We also note that the requirement for a subwavelength gap dimension restricts its sensitivity to submicron transport lengths that are crucially important and generally inaccessible optically. Furthermore, we develop a consistent BTE-based approach for reconstructing the MFP distribution from the experimental data based on a generalization of the suppression function method proposed in Ref. 49. We demonstrate the reconstruction of phonon MFP distributions in single crystalline silicon at different temperatures without any fitting parameters or calibration procedures. The resulting phonon MFP spectra agree reasonably well with first-principles calculations. The experimental simplicity combined with the straightforward analysis algorithm makes our approach applicable to a wide range of materials at the nanoscale.

3.1 Structure Design and Optical Simulation

The sample structure, as shown previously in Fig. 2-1(a), consists of an array of closely spaced metal lines of various line widths sitting on top of the substrate under study. This experimental geometry is much simpler than the 2D hybrid nanostructure developed previously in our group [13]. To avoid direct substrate heating due to laser transmission through the openings between neighboring metal lines, we keep the spacing between neighboring lines to be approximately constant at 150 ~ 200 nm, much smaller than the laser wavelength (~ 790 nm, to be discussed later), while systematically varying the heater size (defined by the metal line width). This sample structure differs from previously used structures in that prior experimental studies typically kept the filling fraction (defined as the ratio of the grating line width to the grating period) constant [7], [13].

To examine the laser energy transmission to the substrate surface, we performed optical simulations using COMSOL Multiphysics software package [99] to obtain the laser transmittance through a metal grating. As shown in Fig. 3-1(a), the simulation domain consists of an aluminum grating on a sapphire substrate, mimicking the experimental sample configuration. Floquet boundary conditions describing the periodicity are used for the periodic boundaries of the simulation domain [99]. We chose sapphire as the substrate underneath the aluminum metal grating since sapphire is transparent in our laser spectrum and allows us to directly compute the transmittance through the metal grating. The materials' optical properties used in the simulation are listed in Table 3.1. The wavelength is specified to be the center wavelength of our laser spectrum, 785 nm. In order to minimize laser transmittance, the polarization of the laser **E** field is specified to be parallel with the metal grating lines to mimic experimental conditions. The angle of incidence is zero (normal incidence). The metal thickness and the gap between neighboring metal lines are set to be 105 nm and 150 nm, consistent with the fabricated grating structures. As suggested by the optical simulation results shown in Fig. 3-1(b), the transmittance through the grating to the substrate is indeed negligible. The optical simulation results, as shown in Fig. 3-1(b), suggest that a spacing of 150 nm is sufficient to achieve negligible direct laser transmission to the substrate. This is expected since the pump and probe wavelengths (~ 785 nm) are much longer than the spacing between neighboring grating lines and the extraordinary transmission phenomenon is not strong in aluminum [100].

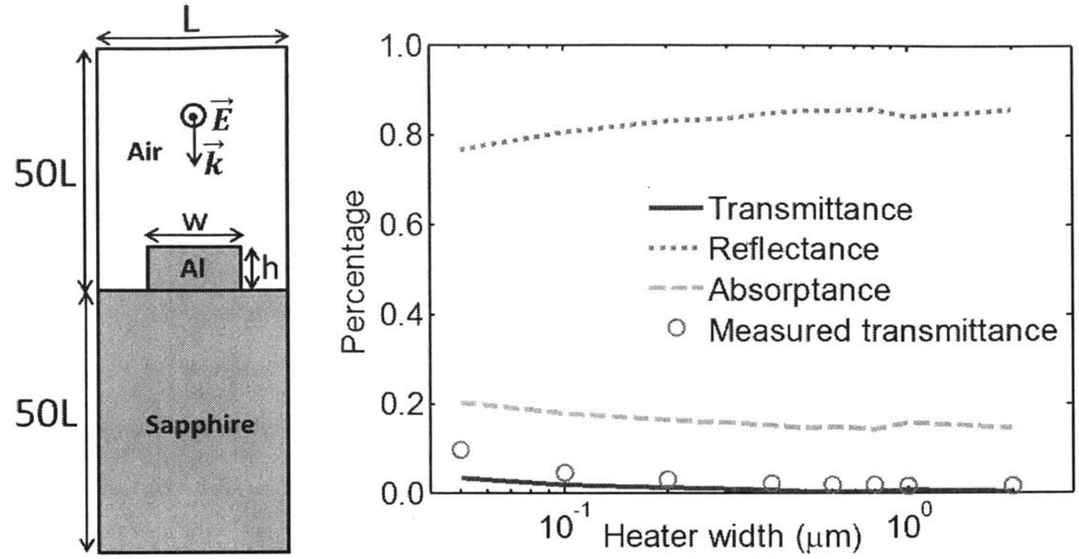

Figure 3-1. (a) Schematic illustration of the optical simulation domain. (b) Simulated and measured transmittance of Al grating on sapphire versus the grating line width.

In addition to optical simulations, we also set up a transmission platform and measured the laser transmittance through the grating structure for different grating line widths. The transmittance setup is sketched in Fig. 3-2. The laser beam first passes through a combination of a quarter wave plate that circularly polarizes the incoming light and a linear polarizer that linearizes the laser polarization in a selected direction. Then the laser beam is focused onto the sample with the patterned metal grating on top. The transmitted laser light is further focused into a photodetector that reads its intensity. The transmittance is defined as the ratio of the transmitted intensity through a metallic grating structure to the transmitted intensity through bare sapphire substrate. The measured transmittance as a function of grating line width, represented by the red circle in Fig. 3-1(b), shows insignificant direct laser energy transmission, suggesting that the designed gratings indeed effectively minimize the laser transmittance to the substrate [101], [102].

Table 3.1 Material optical properties at 785 nm (source: refractiveindex.info).

Material	Refractive index (real part)	Refractive index (imaginary part)
Air	1.00	0.00
Aluminum	2.6265	8.3766
Sapphire	1.7606	0.00

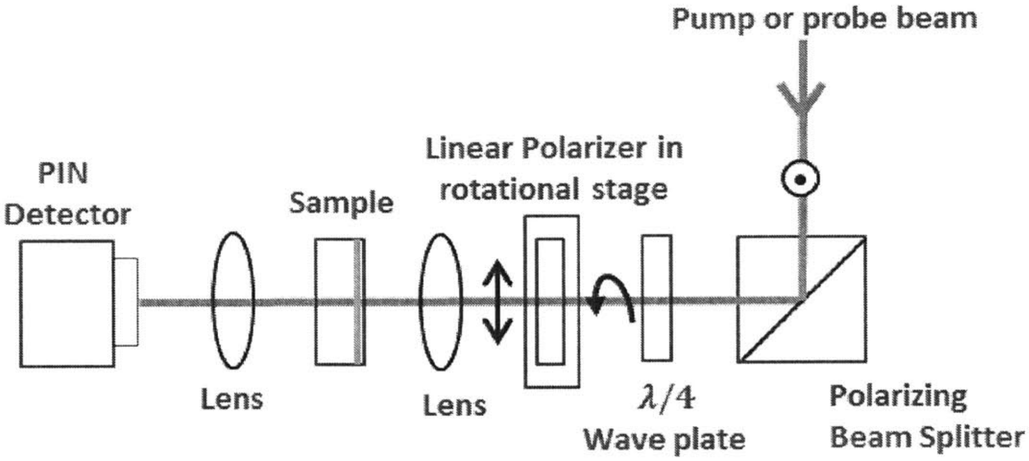
Pump or probe beam
PIN Detector
Sample
Linear Polarizer in rotational stage
Lens
Lens
$\lambda/4$ Wave plate
Polarizing Beam Splitter

Figure 3-2. Schematic diagram of the transmittance measurement setup (built by Dr. Kimberlee C. Collins).

3.2 Sample microfabrication

To demonstrate the wire grid polarizer spectroscopy approach, we choose single crystalline silicon as a benchmark material since its thermal properties have been studied extensively by first-principle DFT calculations. A standard electron beam lithography and liftoff method is used to pattern the gratings onto the substrate. The single crystalline silicon wafers purchased from MTI Corporation are single-side polished and have an area of 10 x 10 mm^2 with 100 crystalline axis. To begin, we use BOE (Buffered Oxide Etch) to etch away the native oxide layer on the silicon substrate. Immediately following the oxide etch, we spin coat a thin layer of electron beam resist 950K A4 PMMA (Polymethyl methacrylate, ~260 nm) onto the substrate. Immediately after resist coating, the sample undergoes prebaking on a hot plate at 180 degree Celsius for approximately 3 minutes. Then the resist is exposed by electron beam at 125 keV using an exposure machine ELIONIX in the Microsystems Technology Laboratory at MIT. After exposure, the resist is subsequently developed using 3:1 IPA:MIBK solution for 90 seconds, followed by an IPA (isopropyl alcohol) rinse and nitrogen blow-dry. We then use an electron beam evaporator to deposit a thin aluminum film onto the silicon wafer. Following metal deposition, we use an acetone bath at room temperature to strip the remaining resist off the silicon substrate. Finally, the sample is rinsed by IPA and blown dry with nitrogen.

Our grating line width varies from 10 μm down to 50 nm, implying a changing filling fraction across gratings with different line widths. The line width and spacing for all the grating patterns were measured using scanning electron microscopy (SEM). The thickness of the metal layers was measured using atomic force microscopy (AFM). Figure 3-3 shows a typical SEM image of a fabricated aluminum grating on a crystalline silicon substrate. Figure 3-4 shows a representative AFM image of the metal thickness measurement for a fabricated metal grating on the crystalline substrate. The metallic gratings act as optical wire-grid polarizers that effectively prevent laser light with polarization parallel to the grating lines from passing through the openings between neighboring lines.

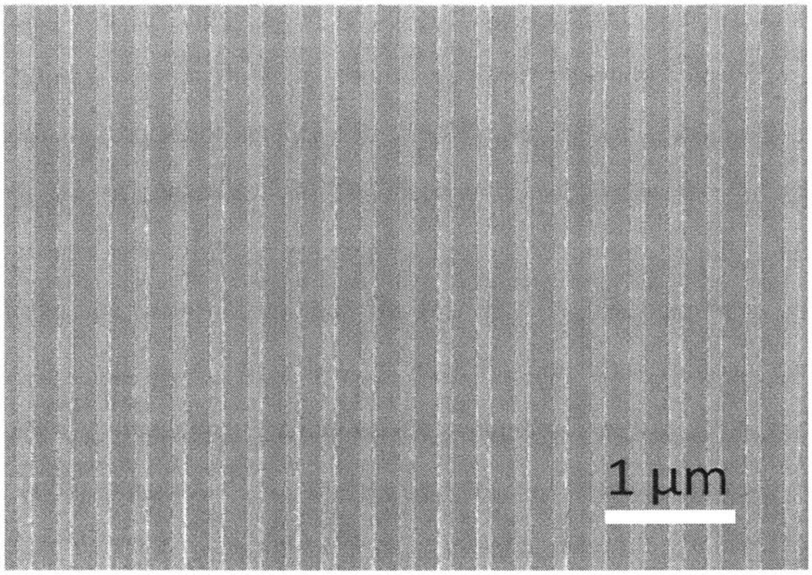

Figure 3-3. SEM image of a typical aluminum grating on silicon substrate.

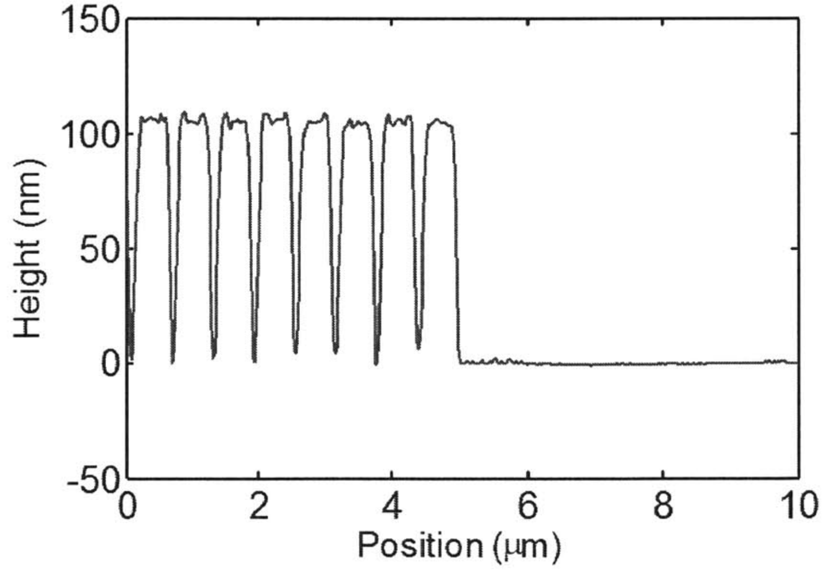

Figure 3-4. AFM measurement of the metal thickness.

3.3 Two-tint Time-domain Thermoreflectance

An ultrafast two-tint TDTR optical setup is used to measure the size-dependent thermal conductivities in this thesis. As discussed in Chapter 1, the original two-color TDTR system in the Rohsenow Kendall Heat Transfer Laboratory, as sketched in Fig. 1-3, uses a second harmonic generator (SHG) optic to double the frequency of the pump beam from 800 nm to 400 nm, therefore the heating wavelength at the sample surface is at 400 nm and the probing wavelength is still at 800 nm [68]. A cold dichroic mirror that reflects blue light and transmits infrared light and a blue color filter are used in combination to separate the pump and probe beams since they have dramatic wavelength difference. For our application, laser transmission through the metallic grating must be minimized to prevent carrier excitation in the substrate. Since the transmittance decreases with increasing wavelength, we modify the original two-color TDTR setup to have infrared pump beam. The modified TDTR setup, called two-tint TDTR and sketched in Fig. 3-5, uses a set of sharp-edge color filters to create spectrally different and distinct pump and probe beams by splitting different part of the Ti:Sapp laser output into the pump and probe arms [71].

Briefly, after passing through an electro-optic modulator (EOM) that enables lock-in signal detection, the pump beam, instead of going through a SHG crystal, goes through two sharp-edged long-pass filters. These two sharp-edged long-pass filters with an edge wavelength of ~ 791 nm are used to cut the short wavelength part of the Ti:Sapp laser spectrum and retain the spectrum with wavelength longer than 791 nm. The pump beam then passes through a quarter wave-plate and a linear polarizer and is subsequently focused by a 10x microscope objective onto the sample surface. After the first PBS, the probe beam passes through a mechanical delay stage that regulates the delay time between the pump beam and the probe beam. A sharp-edged short-pass filter with an edge wavelength of ~781 nm is placed on the probe path to cut the long-wavelength part of the Ti:Sapp laser spectrum and retain the spectrum with wavelength shorter than 781 nm. The probe beam then goes through the quarter wave-plate and the linear polarizer and is focused coaxially with the pump beam onto the sample surface. The combination of the quarter wave-plate and the linear polarizer allows us to control the angle between the laser polarization and the metal grating lines. To create spectrally distinct pump and probe beams and perform reliable measurements, the full-width at half-maximum (FWHM) of the laser source is set to be approximately 12.0 nm [71]. The reflected probe beam from the sample goes through another sharp-edged short-pass filter, which completely rejects the reflected pump beam, before reaching the detector. The lock-in amplifier records the signal as a function of the delay time at the pump modulation frequency. As shown before by the optical simulation and by measuring the thermal response at different angles formed by the laser polarization and the metallic grating, the infrared heating beam indeed significantly reduces the light transmission.

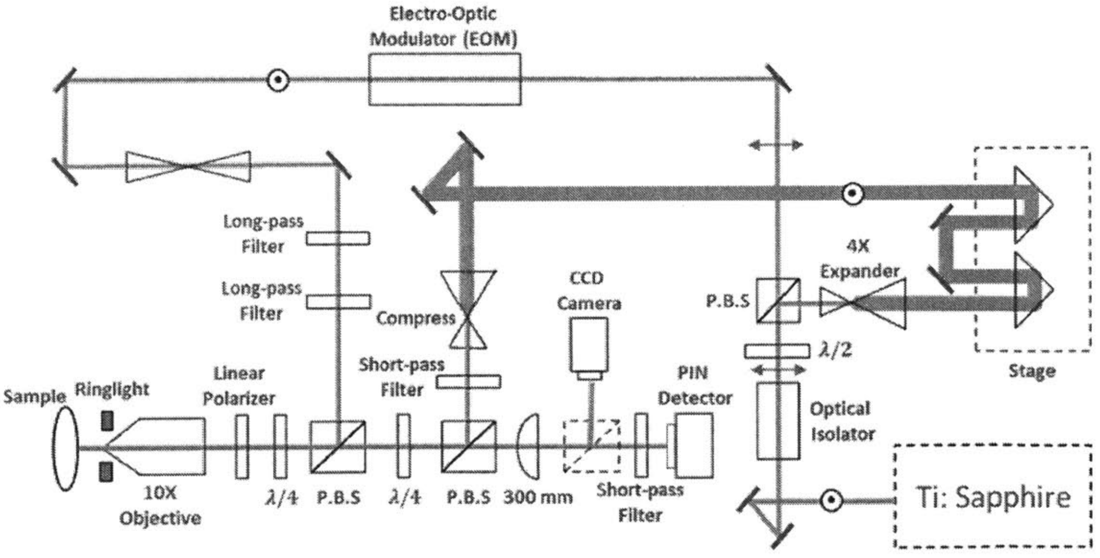
Electro-Optic Modulator (EOM)
Long-pass Filter
Long-pass Filter
Compress
CCD Camera
P.B.S
4X Expander
λ/2
Stage
Sample
Ringlight
Linear Polarizer
Short-pass Filter
PIN Detector
Optical Isolator
10X Objective
λ/4
P.B.S
λ/4
P.B.S
300 mm
Short-pass Filter
Ti: Sapphire

Figure 3-5. Schematic diagram of the two-tint TDTR setup in Rohsenow Kendall Heat Transfer Laboratory at MIT.

3.4 Heat Transfer Model for 1D Grating

In Chapter 1, we gave an overview of the diffusion heat transfer model that is used to describe the thermal transport in the diffusive regime [50], [51], [68]. In this section, we briefly present a modified thermal model to account for the discontinuous nature of the microfabricated metal gratings [47], [98].

When the spacing between neighboring metal lines becomes comparable with the phonon MFPs, the cooling of an individual metal line is affected by the presence of its neighboring lines. In this case, the heaters cannot be viewed as isolated lines and care must be taken to account for the thermal interactions between them. Since the metal line width is typically much smaller than the heating and probing laser spot sizes, we assume a 1D rectangular intensity profile for both pump and probe beams, mimicking the profile of the grating structure. To account for the discontinuous nature of the metal transducer, we assume that the metal has zero diffusivity in the xy-plane and thus heat can only diffuse in the z direction. Under these assumptions, the frequency response function $H(\omega)$ can be derived from solving the conduction heat equation in the frequency domain in the Cartesian coordinate system. The definition of parameter q is slightly modified in the Cartesian coordinate system being that $q = \sqrt{\frac{\sigma_{xy}k_y^2+C_v j\omega}{\sigma_z}}$, where σ_{xy} is the xy-plane thermal conductivity and k_y is the Fourier transform variable in the y-direction perpendicular to the metal grating. The final frequency response is given by [98]:

$$H(\omega) = \sum_n |X_n|^2 (-\frac{D}{C})_n \tag{3-1}$$

where C and D are the matrix elements determined by the material properties, and X_n is the Fourier transform coefficients of the 1D rectangular heating and probing profile, as given by:

$$X_n = \begin{cases} \frac{w}{L}, & n = 0 \\ \frac{1}{2\pi n j}\left(1 - e^{-jn\Omega_0 w}\right), & n \neq 0 \end{cases} \tag{3-2}$$

where w is the grating line width, L is the grating period, and j is the imaginary number $j = \sqrt{-1}$, $\Omega_0 = \frac{2\pi}{L}$ is the fundamental spatial frequency, n is the index for evaluating the spatial Fourier transform frequency at $k_y = n\Omega_0$.

3.5 Measurement Results and Discussion

The two-tint TDTR setup with 791 nm pump and 780 nm probe wavelengths is used for the thermal conductivity measurements. Both the pump and probe beams are linearly polarized with their **E** fields parallel to the metallic grating to ensure that the measured thermoreflectance signal comes only from the metal grating. The substrate effective thermal conductivity and the interfacial thermal conductance between the metal transducer and the substrate are extracted by fitting the experimental reflectance signal with the model prediction based on the heat diffusion theory.

We first measure the effective thermal conductivity of a single crystalline silicon sample at various temperatures using a 30 μm pump spot size on a continuous aluminum transducer film. Figure 3-6 shows the comparison of temperature-dependent silicon thermal conductivities from TDTR measurements [103], DFT calculations and literature [104], [105]. We refine our DFT calculation reported before [36] by using a much finer k mesh in the reciprocal space and the computed thermal conductivities are consistent with the literature data for the entire examined temperature range. Above 200 K, our measurement results agree well with literature and prior TDTR measurements [103] (Ref. 103 used 25 μm pump diameter). However, below 200 K, our measured thermal conductivities fall below the literature value due to non-diffusive thermal transport induced by the finite pump spot size [106] and again agree well with prior measurement data [103].

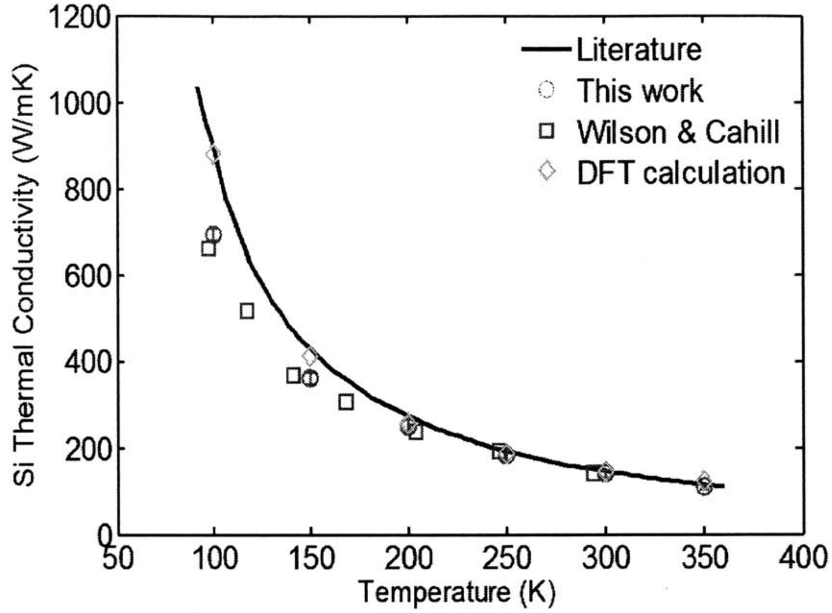

Figure 3-6. Measured silicon thermal conductivities (circles and squares), DFT computed thermal conductivity (diamonds), and the literature data (solid line, Ref. 104).

We then proceed to measure the heater-width-dependent thermal conductivities of silicon samples with aluminum gratings at different temperatures. Since the heating laser spot diameter is typically orders of magnitude larger than the grating line width, the diffusion heat transfer model used for the grating samples assumes two-dimensional thermal transport in the plane perpendicular to the metal grating and accounts for both the heater line width and the spacing between neighboring heaters. Representative traces of the measured phase signals at room temperature and the corresponding model fits for 50 nm, 220 nm and 2 μm heater widths are shown in Fig. 3-7. The fitting quality is excellent for all the heater line widths, indicating that our heat transfer model incorporating an modified substrate thermal conductivity and interface conductance describes well the thermal transport occurring in the TDTR experiments. The effective thermal conductivity decreases dramatically with decreasing heater width. At a very large heater width (2 μm), the measurement returns an effective silicon thermal conductivity very close to the bulk value, indicating diffusive thermal transport in the substrate. At a 220 nm heater width, the effective thermal conductivity is approximately 82% of the bulk value, which suggests that the transport becomes quasiballistic and the experiment measures an additional ballistic resistance [7], [8], [13]. The quasiballistic effect becomes stronger with decreasing heater width, as verified by the constantly decreasing effective thermal conductivity. At a 50 nm heater line width, the thermal conductivity drops to ~ 46% of the bulk value. We note that the observation of near-diffusive transport when $w = 2$ μm does not suggest the maximum phonon MFP in silicon is less than 2 μm since the onset of the quasiballistic transport depends upon the heater line width, the filling fraction of the heater array and the phonon MFP distribution [85].

The effective thermal conductivities of silicon versus heater line width at four different temperatures (circle: 200 K; square: 250 K; triangle: 300 K; diamond: 350 K) are shown in Fig. 3-8. At room temperature, the transition from diffusive transport to non-diffusive transport occurs around 1 μm, below which length scale non-diffusive transport effect becomes increasingly stronger with decreasing heater width. Again, the observed diffusive transport above 1 μm originates from the weak sensitivity of the current measurement approach to probe MFPs larger than several microns and does not indicate that the intrinsic phonon MFP in the sample is less than 1 μm, as will be discussed later. In fact, earlier measurements at room temperature [9], [13] and reduced temperatures [8] have shown that silicon exhibits non-diffusive transport at length scales significantly greater than 1 μm. To a first approximation, phonons in the silicon substrate can be divided into two groups: a diffusive group with MFPs shorter than the heater width and a ballistic group with MFPs longer than the heater width[81]. The observed increasing ballistic resistance originates from an increasingly larger portion of phonons joining the ballistic group as the heater width is reduced. Varying the heater line width in a systematic manner helps sample different MFP phonons' contribution to thermal transport, making it possible to extract the phonon MFP distribution information from the size-dependent thermal conductivities.

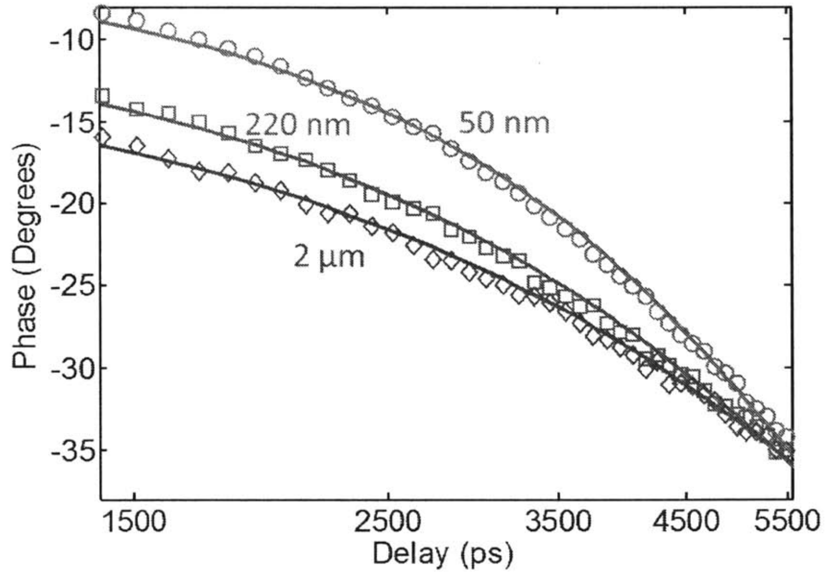

Figure 3-7. Representative traces of measured room temperature TDTR reflectance signals (circles) and best model fits (solid lines) for three heater widths: 50 nm, 220 nm, and 2 µm. The effective thermal conductivities for these three samples are approximately 66.0 W/mK, 120.0 W/mK, and 140.0 W/mK, respectively.

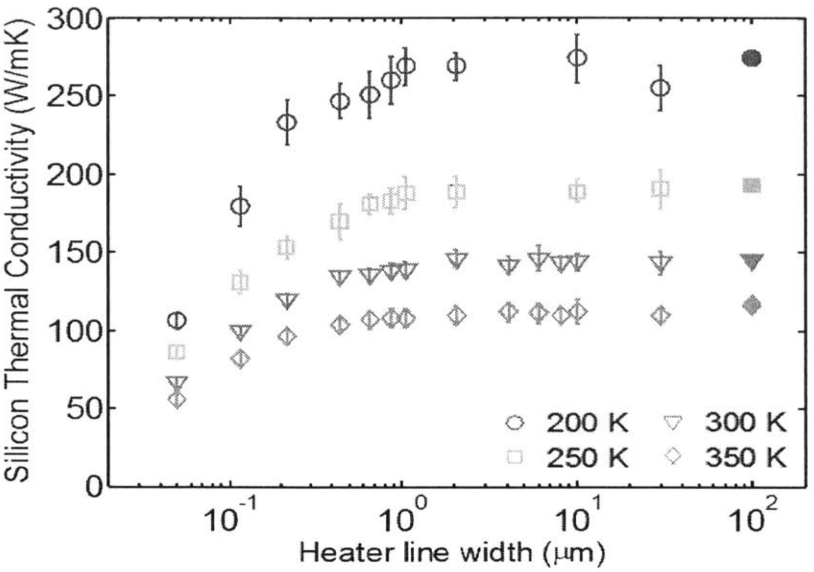

Figure 3-8. Silicon effective thermal conductivities versus heater width at 200 K, 250 K, 300 K and 350 K, respectively. The error bars represent standard deviations in the measured thermal conductivities. The filled dots represent silicon bulk thermal conductivity from literature (Ref. 104) at four different temperatures (circle: 200 K; square: 250 K; triangle: 300 K; diamond: 350 K).

In addition to the optical simulations and transmittance measurement discussed before, we experimentally verify the insignificant direct laser transmittance by varying the laser polarization angle relative to the metal grating and measuring how the reflectance signal changes with varying angles. The angle variation leads to variation in the transmitted laser energy into the substrate through the openings between neighboring metal lines. In principle, as the angle increases, a larger portion of the linearly polarized laser energy directly penetrates into the substrate, resulting in an increasing substrate heating effect. Figure 3-9 compares the room-temperature two-tint TDTR signals at different polarization angles obtained from the grating with the smallest (50 nm wide) aluminum line width on a silicon substrate with linearly polarized laser illumination. Zero degree means that the laser polarization is aligned with the metal grating line. The inset shows the early delay-time reflectance signals. Interestingly, the two-tint signals overlap excellently within

30 degree of angle variation and show a clear thermal decay profile. This experimentally confirms that the impact of direct substrate heating and carrier excitation is negligible at zero-degree angle illumination.

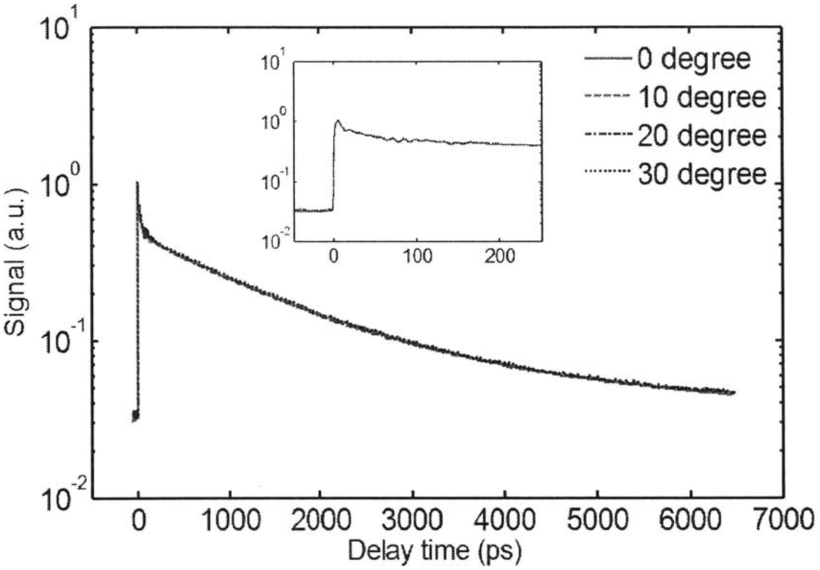

Figure 3-9. Two-tint TDTR signal as a function of the angle between laser polarization and the metal grating lines for the 50 nm line width grating on silicon substrate.

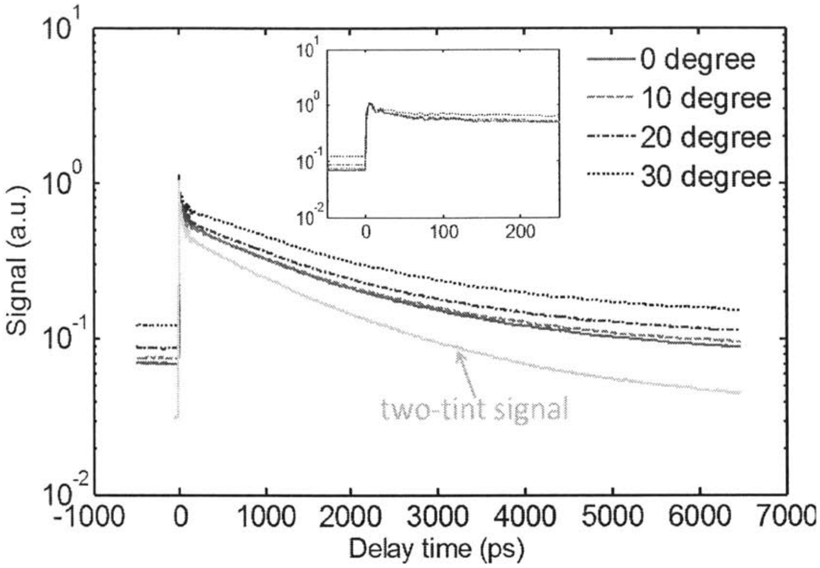

Figure 3-10. Two-color TDTR signal as a function of the angle between the laser polarization and the metal grating lines for the 50 nm wide grating on silicon substrate.

On the other hand, we perform two-color TDTR [51] (pump wavelength = 400 nm, probe wavelength = 800 nm) measurements with linearly polarized beams on the same 50 nm wide grating sample. As shown in Fig. 3-10, the two-color reflectance signal decays much more slowly than the two-tint signal and rises significantly as the angle increases. This arises because a significant portion of the incident blue laser energy in the two-color TDTR experiments directly enters and heats the substrate and excites electron-hole pairs, resulting in a much slower decay profile due to the smaller temperature difference between the metal grating and the substrate. The heating and excitation become stronger when the angle between the blue laser polarization and the metal grating is increased due to an increased amount of direct laser transmission. The fitted thermal conductivity from two-color TDTR measurements on the 50 nm wide grating sample is approximately 17.0 W/mK at zero degree and decreases constantly as the angle is increased. It is clear that the thermal conductivities derived from the two-color signals, as affected by the direct substrate heating and electron-hole pair generation, are remarkably lower than those derived from two-tint signals (~66 W/mK), and thus do not reflect the real non-diffusive thermal transport effects physically induced purely by the finite heater line width since the diffusion heat transfer model used to fit the experimental signal does not account for direct heating and electron-hole pair generation in the substrate. Moreover, the thermal conductivities derived from the two-tint signals have a weak angle dependence within 30 degree of angle variation, again confirming the insignificant direct substrate heating. For heater line width larger than 50 nm, the reflectance signals measured by the two-tint TDTR overlap quite well even for an angle variation larger than 30 degree due to lower laser energy penetration into the substrate relative to heating of the metal lines.

3.6 MFP Reconstruction

To gain insight into which phonon MFPs are responsible for heat conduction in the substrate, we follow the reconstruction approach proposed by Minnich [49]. To extract the intrinsic phonon MFP distribution from the measured length-dependent thermal conductivities k_{eff}, Minnich[49] introduced a heat flux suppression function to relate the measurement results to the MFPs:

$$k_{eff}(w) = \int_0^\infty S(\eta) f(\Lambda) d\Lambda = \int_0^\infty -\frac{dS}{d\eta}\frac{d\eta}{d\Lambda} F(\Lambda) d\Lambda \qquad (3\text{-}1)$$

where $\eta = \frac{\Lambda}{w}$ is the ratio of the spectral MFP to the characteristic thermal length w, $S(\eta)$ is the suppression function, $K(\eta) = -\frac{dS}{d\eta}$ is the kernel function, $f(\Lambda)$ is the differential phonon MFP distribution, and $F(\Lambda)$ is the cumulative phonon MFP distribution. $F(\Lambda)$ is related to $f(\Lambda)$ through: $F(\Lambda) = \int_0^\Lambda f(\Lambda') d\Lambda'$.

Minnich's original formulation of the MFP reconstruction algorithm [49] assumes that the measurement is characterized by a single length parameter w such that the suppression function is a function of the single variable $\eta = \frac{\Lambda}{w}$. This is rarely the case in a real experiment: in fact, the transient grating measurements of thin membranes considered in Ref. 49 involved two characteristic lengths, i.e. the membrane thickness and the transient grating period. Likewise, our experiments involve two characteristic geometric lengths: the heater line width w and the array period L. However, the approach developed by Minnich[31] can be used in a more general way not requiring that the suppression function for all measurements be given by a single function of a single nondimensional variable. Consider N measurements on the same or different samples, with an effective thermal conductivity k_i in the *i-th* measurement described by the suppression function $S_i(\eta)$:

$$k_i = \int_0^\infty S_i(\eta) f(\Lambda) d\Lambda = S_i^\infty + \int_0^\infty K_i(\eta) \frac{d\eta}{d\Lambda} F(\Lambda) d\Lambda \qquad (3\text{-}2)$$

where $K_i(\eta)$ is the kernel function for the i-th measurement. The second equality is obtained through integration by parts and note that $F(0) = 0$ and $F(\infty) = 1$. Thus we generalize Minnich's equation presented earlier by allowing the suppression function to be different for each measurement (the possibility of such generalization has been in fact pointed out by Minnich [49]). A further generalization is made by allowing the suppression function to have nonzero residual suppression at the limit of large Λ: $S_i(\Lambda \to \infty) = S_i^\infty$. Although the residual suppression factor is zero for some experimental configurations, it can be finite and significant for other geometries, such as the ones used in this work as discussed below.

The suppression functions for our sample geometries depend on two nondimensional variables: the ratio of MFP to heater width $\eta = \frac{\Lambda}{w}$ and filling fraction $\mathrm{FF} = \frac{w}{L}$, where L is the heater array period. The filling fraction takes into account the impact of the heater array periodicity on the heat transfer regime in the underlying substrate. The relevant suppression function for the measurement on sample i with filling fraction FF_i is $S_i = S(\eta, \mathrm{FF}_i)$. The suppression functions are calculated from the gray-body phonon BTE in Chapter 2 and are combined with the measurement results in this Chapter to determine the MFP distributions.

The computed suppression functions across a range of filling fractions, as shown in Fig. 3-11, capture the transition from totally diffusive transport regime to strongly ballistic transport regime. In the diffusive limit, all the phonons contribute to thermal conductivity as described by the heat diffusion theory and the suppression factor is unity regardless of the filling fraction, whereas in the non-diffusive limit, long-MFP phonons' contributions to heat transport are suppressed and the suppression factor depends on both the ratio of MFP to heater width $\frac{\Lambda}{w}$ and the filling fraction FF. Depending on the spacing between neighboring heaters, thermal transport in the substrate external to the heater array may differ significantly from highly ballistic heat spreading from an isolated nanoscale hot spot [12], [85]. Given the heater size, the thermal transport near an individual heater is weakly affected by the presence of its neighboring heaters in the case of small filling fraction, whereas for a large filling fraction, the thermal transport near one heater is strongly influenced by the presence of neighboring heaters. The BTE simulation returns the bulk substrate thermal conductivity for a continuous film heater (FF = 100%) that can be viewed as a superposition of an infinite number of isolated point heat sources on the substrate, suggesting that superposition of closely spaced ballistic heat sources recovers the familiar diffusive transport in the underlying substrate. As the filling fraction approaches 100%, the suppression function approaches unity for all phonon MFPs. Figure 3-8 shows that our measurements yield the bulk thermal conductivity values for $w > 1$ μm, indicating that for filling fractions above 90% the measurements are no longer sensitive to non-diffusive transport. For the same ratio of phonon MFP to heater size, the BTE simulation shows that a smaller filling fraction leads to stronger ballistic transport as demonstrated by Fig. 3-11 [85]. The residual suppression function value that occurs when the phonon MFP is much larger than the heater width increases toward unity with increasing filling fraction. Figure 3-11 clearly shows that phonons with MFPs longer than the heater line width still carry significant amount of heat. In fact, our results show that significant residual suppression exists for finite filling fractions even when $\frac{\Lambda}{w}$ approaches infinity.

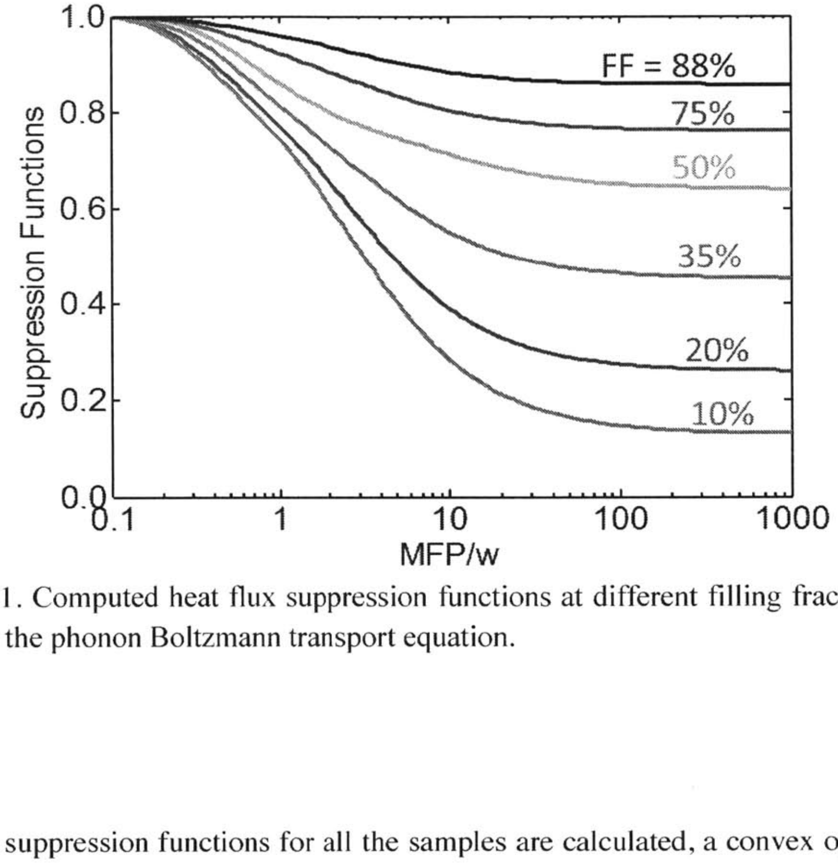

Figure 3-11. Computed heat flux suppression functions at different filling fractions based on solving the phonon Boltzmann transport equation.

After suppression functions for all the samples are calculated, a convex optimization scheme is used to reconstruct the phonon MFP distribution [49], [54]. For our sample geometry, the kernel functions, as shown in Fig. 3-12, span just under two orders of magnitude from approximately $\frac{\Lambda}{w} = 0.1$ to $\frac{\Lambda}{w} = 5$, meaning that the thermal conductivity measurement for a certain heater width w contains MFP distribution information ranging from approximately one tenth of the heater width to five times that of the heater width. Since our minimum heater line width is 50 nm, our MFP reconstruction scheme is sensitive to the cumulative MFP distribution much smaller than 50 nm (down to ~ 5 nm).

Figures 3-13 to 3-16 compare the reconstructed silicon MFP distributions at four different temperatures with DFT calculations using a very dense k mesh (64 x 64 x 64 k meshes) in the reciprocal space [107]. The reconstructed phonon MFP distributions agree well with DFT predictions for all the studied temperatures. The agreement demonstrates the viability of the current thermal conductivity spectroscopy technique.

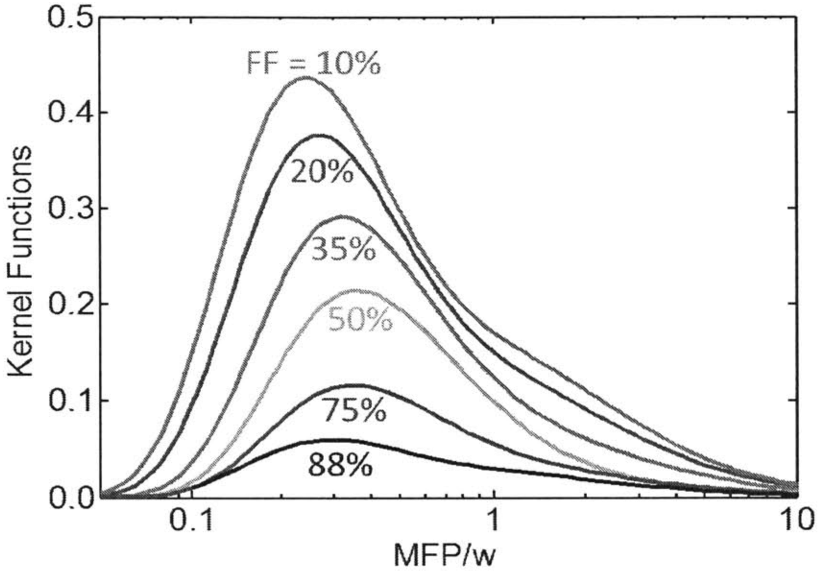

Figure 3-12. Computed kernel functions versus filling fractions.

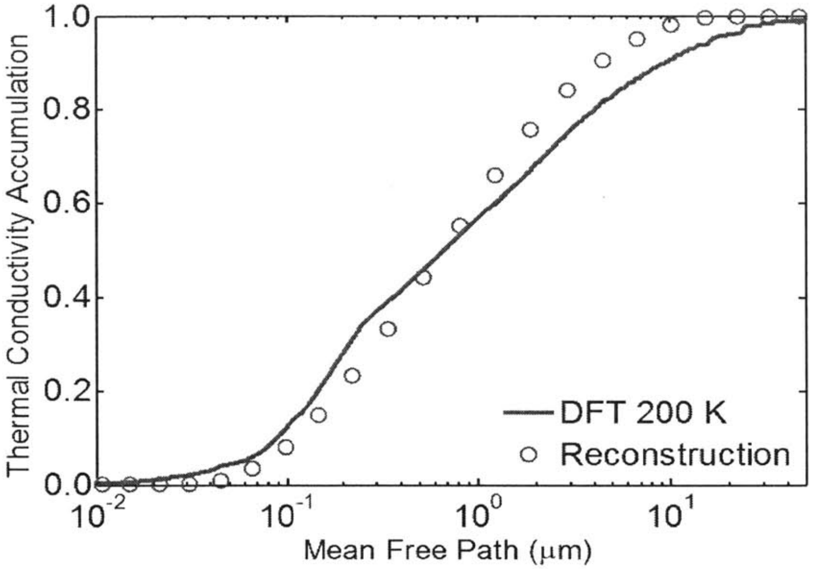

Figure 3-13. Comparison of experimentally reconstructed silicon MFP distributions and predictions from DFT calculations at 200 K.

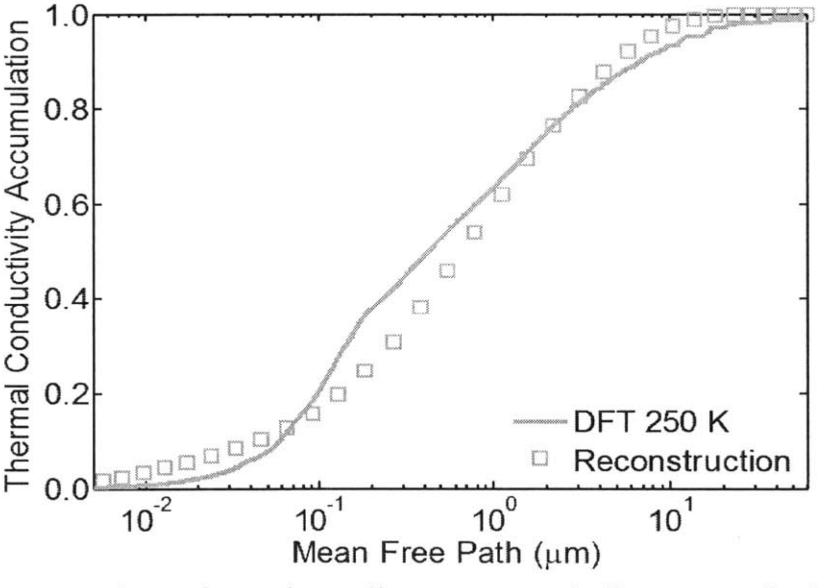

Figure 3-14. Comparison of experimentally reconstructed silicon MFP distributions and predictions from DFT calculations at 250 K.

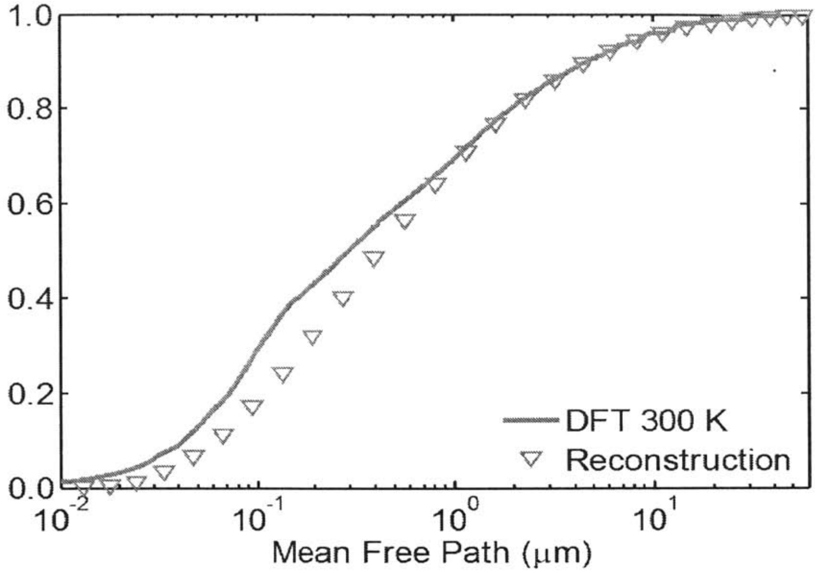

Figure 3-15. Comparison of experimentally reconstructed silicon MFP distributions and predictions from DFT calculations at 300 K.

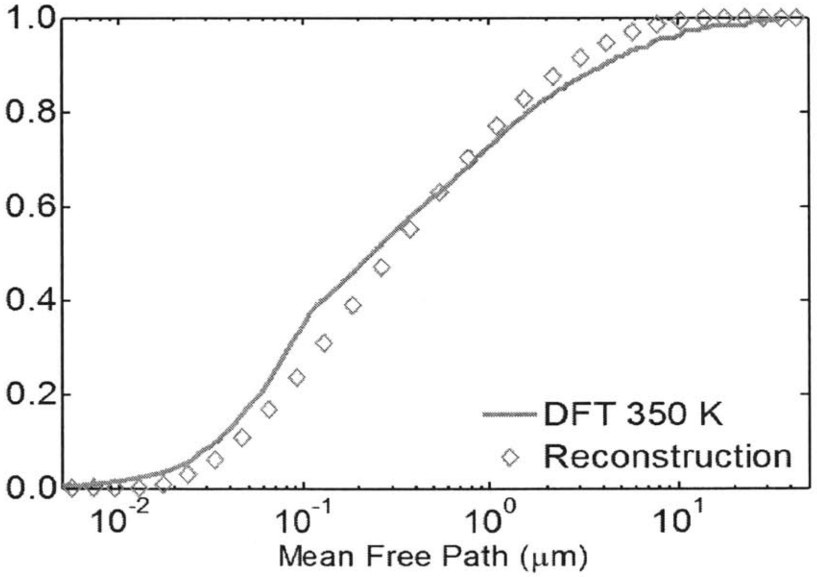

Figure 3-16. Comparison of experimentally reconstructed silicon MFP distributions and predictions from DFT calculations at 350 K.

The described thermal conductivity spectroscopy technique is a general method for studying phonon MFPs in a wide range of materials. The ability to obtain MFP spectra using this approach will lead to a better understanding of microscopic phonon-mediated heat transport in nanostructures and bulk materials and have important implications in many technological applications. Compared to our previous work using hybrid heater nanostructures [13], the current approach utilizing 1D metal gratings greatly simplifies the fabrication processes. Given its sensitivity, our future work will focus on materials of practical interest, such as thermoelectrics. Future design of more efficient thermoelectric devices calls for a more adequate understanding of microscopic thermal transport in thermoelectric materials. As predicted by previous DFT calculations, most thermoelectric materials have dominant phonon MFPs in the a few tens to a few hundreds of nanometers range [31], [44]. Therefore, our approach is well suited for measuring phonon MFPs in those materials for which *ab*-initio calculations are difficult and inaccurate due to the complex material structure. The ability to measure MFP distributions in thermoelectric materials may serve as a blueprint for engineers to tailor thermal conductivity for better device performance [24], [25], [31]. In Chapter 4, we will discuss the progress made towards studying phonon MFP distributions in some select thermoelectrics.

3.7 Summary

We developed a new implementation of a thermal conductivity spectroscopy technique that can be employed to probe phonon mean free paths in opaque materials down to tens of nanometers. The technique utilizes 1D metallic gratings with sub-optical-wavelength gaps between the metal lines to localize the heating to the metal lines and insulate the substrate from linearly polarized laser illumination. We demonstrated the technique by measuring the length-dependent effective thermal conductivities of crystalline silicon at various temperatures using the two-tint time-domain thermoreflectance method. We also generalized the MFP reconstruction scheme to measurements involving multiple characteristic lengths by recognizing the importance of residual suppressions in the limit of infinite phonon MFP, and we developed a consistent BTE-based procedure to extract the MFP distribution from the measured thermal conductivity data. The reconstructed phonon MFPs in silicon agree reasonably well with results predicted from first-principles DFT calculations, without any fitting parameters. The agreement between the reconstructed MFP distributions and the DFT-based calculation results indicates that now we have both experimental and computational tools for studying nanoscale phonon MFPs in a wide range of materials of interest.

Chapter 4

Probing phonon MFP distributions in thermoelectrics

4.1 Thermoelectrics Background

Thermoelectric energy conversion is a solid state technique that can convert heat directly to electricity without any intermediate mechanical steps [23], [24], [28], [31]. Due to its reliability and potential to harvest the vast amount of waste heat from industrial applications, thermoelectrics have gained renewed research interest for the last two decades. The basic principle is based upon the Seebeck effect, discovered by Thomas Johann Seebeck in 1821, that a voltage is generated across the two junctions of a material when those two junctions are subjected to a temperature difference. The generated voltage can be used to produce electricity if a closed-loop circuit is formed. The heat to electricity energy conversion efficiency is characterized by a nondimensional thermoelectric figure of merit *ZT*, defined as $ZT = \frac{S^2\sigma T}{k_p+k_e}$, where S is the Seebeck coefficient, σ is the electrical conductivity, T is the average operating temperature, k_p and k_e are the lattice and electronic contribution to thermal conductivity, respectively. The product, $S^2\sigma$, is termed power factor since it is related to the power output density for a given thermoelectric device. The higher the *ZT*, the higher the energy conversion efficiency.

The challenge associated with improving *ZT* is that thermal and electrical properties are generally highly inter-coupled [1], [108], [109]. Improving one material property in a favorable direction often times causes changes in other properties that adversely affect the overall *ZT*. For example, one might think of increasing the doping level to enhance the electrical conductivity, but this typically leads to a reduction in the Seebeck coefficient and an increase in the electronic thermal conductivity that may counteract the effect of enhancing the electrical conductivity. One common practice over the last two decades to improve *ZT* is to use nanostructuring approach [110], [111], proposed by Hicks and Dresselhaus, that can significantly reduce the lattice thermal conductivity while maintaining the electrical properties unchanged. The achieved reduction in the lattice thermal conductivity results mainly from the additional phonon interface or phonon boundary scattering induced by the introduction of nanometer scale structures [22], [25]–[27], [112]. These additional scattering events effectively shorten the phonon MFPs that contribute to thermal conductivity and thus improve the thermoelectric performance [113].

Although the nanostructuring approach has been proved effective in enhancing the figure of merit *ZT* by reducing the heat-carrying phonon MFPs, quantitative knowledge of the phonon MFP distributions is still limited, even for the majority of the bulk thermoelectric materials. First-principle DFT has been used to compute the phonon MFP distributions in some select thermoelectric materials with relatively simple atomic structures [37], [39], [44], but for complex thermoelectric materials such calculation is still prohibitive. Engineering the next generation thermoelectric materials calls for a more fundamental understanding of the distribution of the heat-carrying phonon MFPs. Knowing the phonon MFP distributions in thermoelectric materials would guide the design of next-generation thermoelectrics towards a higher level of *ZT*. For example, one might be able to optimize the size distribution of the nanoscale structures to optimally scatter phonons of different MFPs [114].

In Chapter 3, we demonstrated the feasibility of the wire grid polarizer approach to measuring phonon MFP distributions indirectly in opaque samples. In this Chapter we apply the same approach to probe the phonon MFP distributions in some select thermoelectric samples. The materials we study include a half heusler sample $Nb_{0.95}Ti_{0.05}FeSb$ [115] and a boron-doped nanocrystalline $Si_{80}Ge_{20}B_{2.5}$ sample [116]–[118]. We choose $Nb_{0.95}Ti_{0.05}FeSb$ as a first try because recent experimental studies observed a record high power factor in that sample compared with other semiconductor-based thermoelectric materials [119]. We would like to study its phonon MFP distribution to gain more understanding on its microscopic thermal transport. Nanocrystalline $Si_{80}Ge_{20}B$ sample is chosen to investigate the quantitative impact of grain boundary scattering on the phonon MFP spectrum [116]–[118]. After obtaining the length-dependent thermal conductivities, we use the same reconstruction algorithm to extract the phonon MFP distributions in both materials. The reconstructed MFP distributions shed light on the dominant heat-carrying phonon MFPs in those materials and may also guide the design of next generation thermoelectric materials and devices to achieve better energy conversion performance. The extracted MFP distribution for nanocrystalline $Si_{80}Ge_{20}B_{2.5}$ sample also helps us gain insight into the impact of phonon-grain boundary scattering on the heat carrying phonons' MFPs.

4.2 Sample preparation and pattern fabrication

The thermoelectric samples were provided from Professor Zhifeng Ren's group at the University of Houston [115]. To prepare the samples, ingots were first formed by arc melting individual elements contained in the samples. To guarantee uniformity, the ingots were melted a few times and flipped over each time. The ingots were then ball milled for a few hours to produce nano powders that were subsequently hot pressed under high temperatures and high pressures to produce sample disks of half-inch diameter. Figures 4-1(a) and 4-1(b) show the SEM image of the grain structures in $Nb_{0.95}Ti_{0.05}FeSb$ and $Si_{80}Ge_{20}B_{2.5}$, respectively.

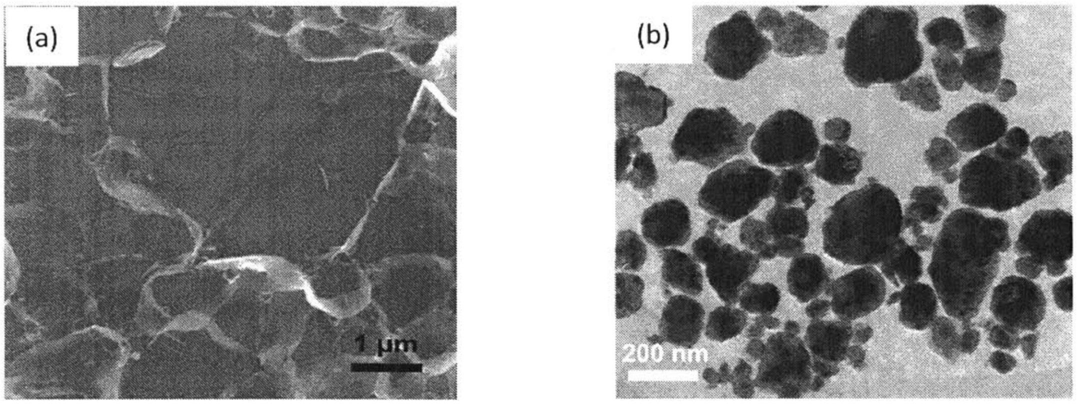

Figure 4-1. SEM images of grain structures in (a) $Nb_{0.95}Ti_{0.05}FeSb$ (Courtesy of Mr. Ran He) and (b) $Si_{80}Ge_{20}B_{2.5}$, respectively. Figure 4-1(b) is adapted from Ref. 116.

The as-received samples typically have rough surfaces that cannot be directly used to perform microfabrication and TDTR measurement. To improve the surface quality, we developed a polishing process following Dr. Collins's recipe to mechanically polish the samples until a desired root mean square (RMS) roughness is achieved [98], [120], [121].

The polishing is done on a South Bay Technology lapping and polishing machine (model 920) that contains a central rotary lapping plate and a yoke that provides additional rotation to the sample holder. To start, the recipe uses a set of SiC grinding papers, 200-400-600-800-1200 grit in sequence, to planarize and smooth the as-diced sample surface. Each step takes approximately 5-10 mins and the sample is thoroughly rinsed by DI water between each polishing step. The surface normally has mirror finish after the 1200 grit grinding paper polishing.

Following the grinding paper polishing, the sample is then polished using 1um Al_2O_3 or diamond suspension on a hard polishing cloth (Buehler Trident) for about 10mins. To fine-polish the sample surface, we dilute the 50nm Al_2O_3 suspension with DI water until the pH of the diluted suspension reaches ~7.5. A two-step fine polishing procedure is used to obtain an excellent surface finish. First, we use the prepared suspension to polish the sample on a hard cloth (Buehler Trident) for approximately 10mins with continuous feeding of the suspension. Then, the sample undergoes a final polish on a soft polishing cloth (Buehler Microcloth) for about 15secs. As mentioned in Ref. 98, the final polishing time is critical to achieve an excellent surface finish without pits or orange-peel texture. The sample is thoroughly rinsed by warm DI water to remove any residual polishing suspension on top of the surface and is then blown dry.

The developed recipe can routinely achieve a surface finish with RMS roughness around or less than 5 nm. Figure 4-2 shows a representative atomic force microscopy (AFM) image of the surface roughness on a 5 um x 5 um area with RMS roughness $R_q \sim 6$ nm and arithmetic roughness $R_a \sim 4$ nm on a $Nb_{0.95}Ti_{0.05}FeSb$ sample.

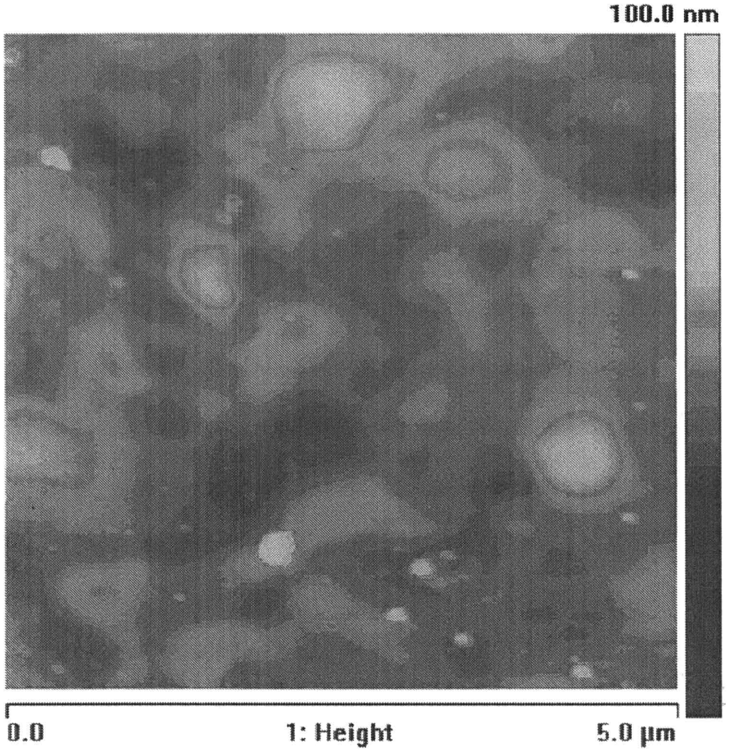

Figure 4-2. A representative AFM image of the surface roughness for a 5 um x 5 um polished $Nb_{0.95}Ti_{0.05}FeSb$ area. The RMS roughness R_q and arithmetic roughness R_a are ~6 nm and ~ 4 nm, respectively.

Following the polishing process, the sample is patterned with grating nanostructures in order to perform size-dependent thermal conductivity measurement. We follow a lithography recipe similar to the one used for single crystalline silicon substrate to fabricate aluminum gratings of variable linewidths on top of the polished thermoelectric samples. Figure 4-3 shows a representative SEM image of the fabricated metal grating on top of the $Nb_{0.95}Ti_{0.05}FeSb$ substrate.

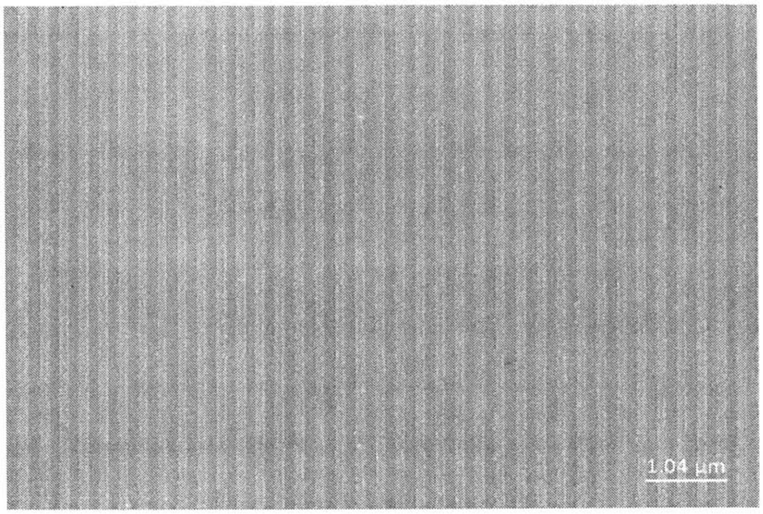

Figure 4-3. A representative SEM image of the fabricated metal grating on the $Nb_{0.95}Ti_{0.05}FeSb$ substrate.

4.3 Thermal conductivity measurement

Following the sample microfabrication, we again use the two-tint TDTR setup to measure the length-dependent thermal conductivity for the prepared samples. Figure 4-4 shows a representative fitting for the $Nb_{0.95}Ti_{0.05}FeSb$ substrate at three different heater sizes at room temperature. The circles represent the experimental measurement phase data and the blue curves represent the best fittings based on a diffusion heat transfer model with a modified substrate thermal conductivity. As shown in Fig. 4-4, the fitting quality appears to be very good, indicating that the diffusion heat transfer model with a modified effective thermal conductivity can describe the thermal transport in the TDTR measurement. The green and red dashed curves in Fig. 4-4, representing a 10% bounds on the best-fitted thermal conductivity, show the sensitivity of the fitting to the substrate thermal conductivity. It is clear that the fitting is pretty sensitive to the thermal conductivity we would like to extract from the experimental data.

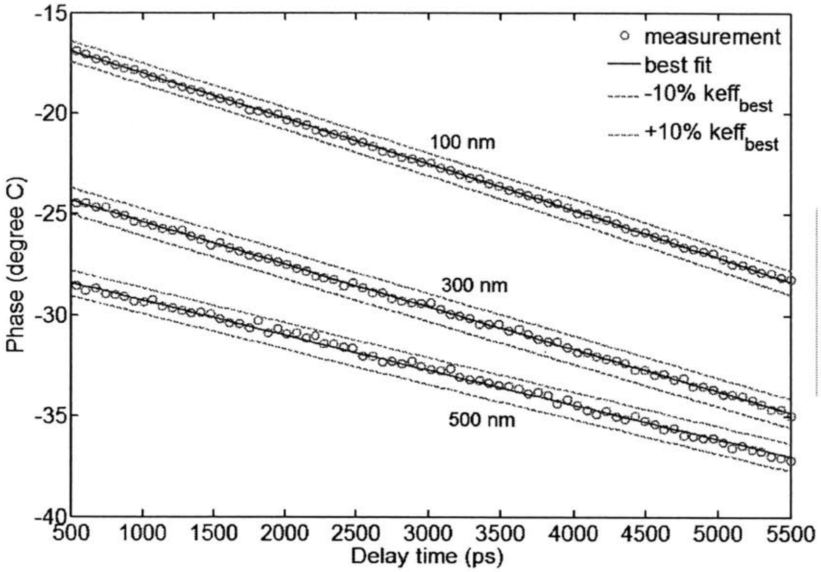

Figure 4-4. Representative TDTR fittings for the $Nb_{0.95}Ti_{0.05}FeSb$ substrate at three different heater sizes.

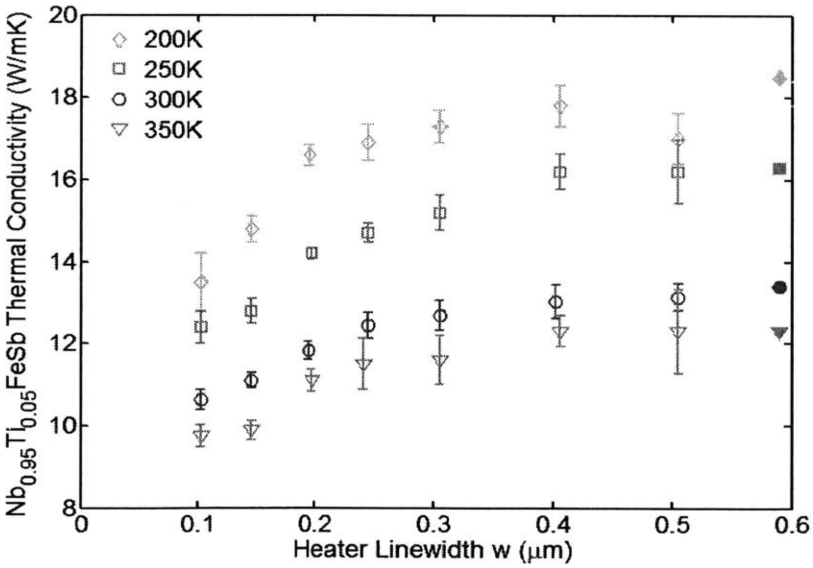

Figure 4-5. Measured size-dependent $Nb_{0.95}Ti_{0.05}FeSb$ thermal conductivities across a range of temperatures. The filled dots represent the bulk thermal conductivity at the corresponding temperatures.

Figure 4-5 shows the measured length-dependent thermal conductivities for the $Nb_{0.95}Ti_{0.05}FeSb$ substrate across a range of lengthscales and temperatures. The filled dots denote the bulk thermal conductivities at corresponding temperatures. As shown in Fig. 4-5, when the heater size is large, the measured thermal conductivity is close to the bulk value, indicating near-diffusive thermal transport. However, the thermal conductivity becomes length-dependent when the heater size is reduced below ~300 nm, implying the transition of the transport from diffusive to non-diffusive regimes. Note that the electronic contribution to thermal conductivity in the $Nb_{0.95}Ti_{0.05}FeSb$ substrate is approximately 10% using the Wiedemann-Franz law and the measured electrical conductivity. Since our interest is to study the phonon MFP distributions, we subtract the electronic thermal conductivity from the measured total thermal conductivity to give the lattice thermal conductivity that is subsequently used in the reconstruction algorithm to approximately extract the phonon MFP distribution. This is justifiable since the electron MFP is much shorter than the heater size and no non-diffusive electron transport is expected.

As mentioned before, nanostructured thermoelectric materials show favorable performance compared with their bulk counterpart. To examine the impact of grain boundary scattering on the thermal phonon MFP spectra in thermoelectric materials, we apply the wire-grid polarizer approach to studying non-diffusive thermal transport in nanocrystalline $Si_{80}Ge_{20}B_{2.5}$ sample that is commonly used in thermoelectric applications at elevated temperatures [28], [31]. In bulk SiGe systems, the introduced impurity significantly scatters the high-frequency, short-wavelength phonon modes and suppresses their contribution to thermal conductivity. Consequently, the fractional thermal conductivity contribution from long-MFP phonons in SiGe can be even larger than that of single crystalline silicon, as shown by prior first-principles calculations [122]. For nanocrystalline SiGe samples, the additional grain boundary scattering can significantly suppress the effective MFPs of the low-frequency phonon modes. Prior experimental studies indeed observed significant reduction in lattice thermal conductivity as the grain size was systematically reduced [116]–[118], [123]. However, few studies focused on the quantitative impact of the grain boundary scattering on the microscopic MFP spectrum [123].

To gain insight into the effect of grain boundary scattering, we study size-dependent thermal transport in boron-doped $Si_{80}Ge_{20}B_{2.5}$ sample. Similar fabrication recipe is used to pattern metallic nanowires on top of the sample. The patterned sample is subsequently characterized using the two-tint TDTR setup. Figure 4-6 shows some representative measurement phase data at three different heater sizes along with the respective best fittings based off the diffusion heat transfer model with a modified thermal conductivity. It is clear that the heat diffusion model with an apparent substrate thermal conductivity can accurately describe the thermal transport in the near-diffusive regime. The measured size-dependent effective thermal conductivities for the nanocrystalline $Si_{80}Ge_{20}B_{2.5}$ sample are shown in Fig. 4-7. Again we observe a clear transport transition from diffusive to non-diffusive regimes when we systematically reduce the heater size. Figure 4-8 compares the normalized size-dependent effective thermal conductivities of Si and $Si_{80}Ge_{20}B_{2.5}$ measured at room temperature. Since grain boundary scattering significantly shortens the effective MFPs of low-frequency phonons in $Si_{80}Ge_{20}B_{2.5}$, the probed degree of non-diffusive thermal transport in $Si_{80}Ge_{20}B_{2.5}$ is generally weaker than that of Si, especially at small heater sizes.

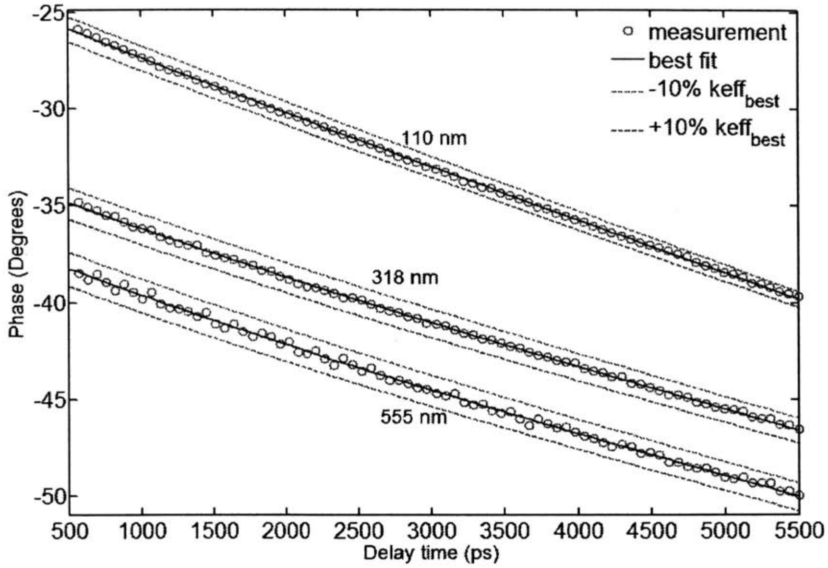

Figure 4-6. Representative TDTR fittings for the $Si_{80}Ge_{20}B_{2.5}$ substrate at three different heater sizes.

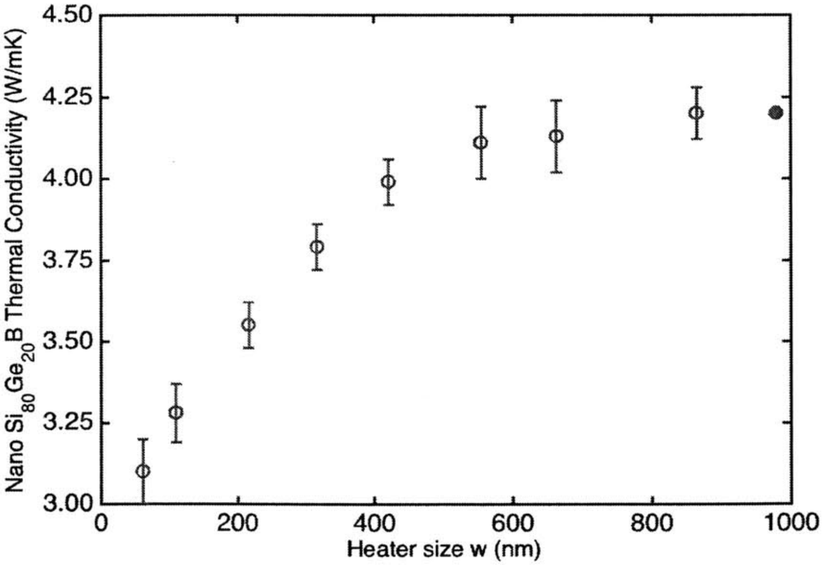

Figure 4-7. Measured size-dependent $Si_{80}Ge_{20}B_{2.5}$ thermal conductivities at room temperature. The filled dot denotes the bulk thermal conductivity.

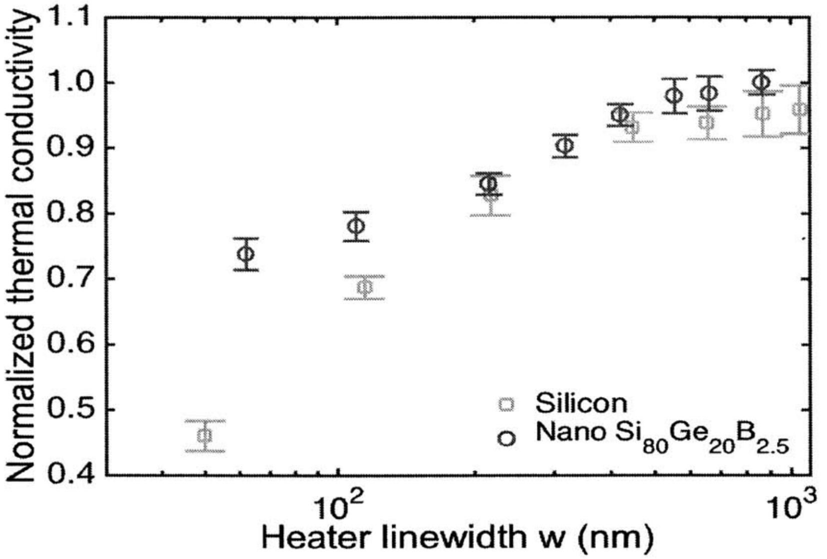

Figure 4-8. Normalized size-dependent effective thermal conductivities of single crystalline Si and $Si_{80}Ge_{20}B_{2.5}$ measured at room temperature.

4.4 MFP reconstruction and results discussion

To gain insight into the distribution of the heat-carrying phonon MFPs, we follow the same reconstruction algorithm described in Chapter 3 to extract the phonon MFP distributions in the studied samples. Figures 4-9 and 4-10 show the reconstructed thermal conductivity accumulation functions for the $Nb_{0.95}Ti_{0.05}FeSb$ sample at two different temperatures and for the nanocrystalline $Si_{80}Ge_{20}B_{2.5}$ sample at room temperature, respectively. As shown in Fig. 4-9 and Fig. 4-10, the dominant heat-carrying phonon MFPs are in the a few tens to a few hundreds of nanometers range for both thermoelectric materials at room temperature. Also shown in Fig. 4-10 are the calculated phonon MFP distributions for single crystalline silicon and bulk $Si_{50}Ge_{50}$ from first principle DFT computation [36], [122]. The comparison clearly shows that nanometer scale grain structures introduced in the nanocrystalline $Si_{80}Ge_{20}B_{2.5}$ sample significantly scatters long-MFP phonons and thus reduces the effective phonon MFPs that contribute to thermal transport. The obtained phonon MFP spectra will provide guideline for designing more efficient thermoelectrics to further enhance the energy conversion performance.

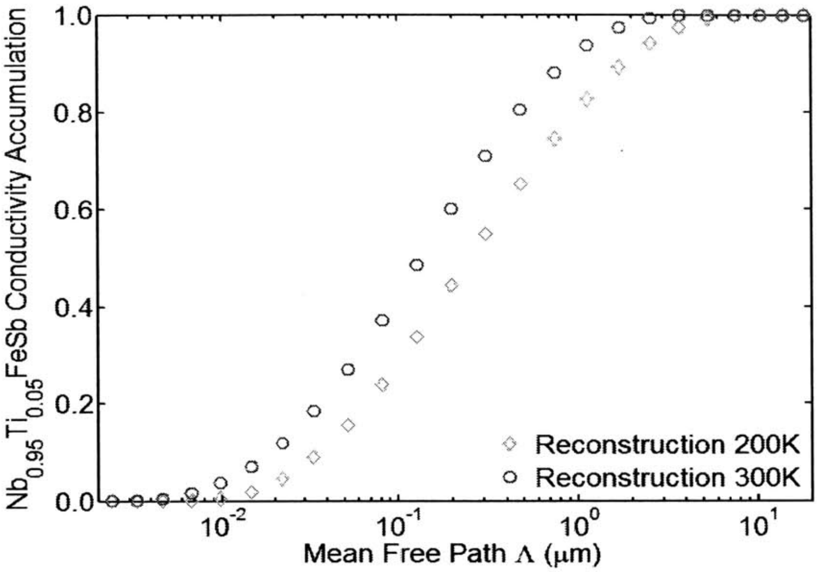

Figure 4-9. Reconstructed phonon MFP distributions for $Nb_{0.95}Ti_{0.05}FeSb$ at two temperatures. The dominant heat-carrying phonon MFPs are in the a few tens to a few hundreds of nanometers.

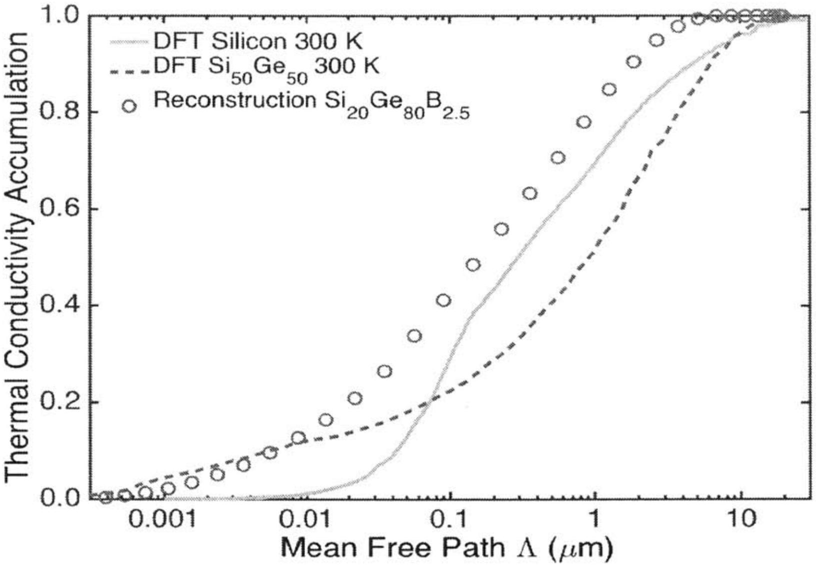

Figure 4-10. Reconstructed phonon MFP distribution for $Si_{80}Ge_{20}B_{2.5}$ at room temperature. The dominant thermal phonon MFPs are in the a few tens to a few hundreds of nanometers. The MFP spectrum comparison clearly shows that grain boundary scattering significantly suppresses the contribution of long-MFP phonons to thermal conductivity.

4.5 Summary

In this chapter we applied the wire grid polarizer spectroscopy approach to study the distribution of phonon MFPs that contribute to the thermal conductivity of some select thermoelectric materials. We developed material-specific polishing recipe and lithography recipe to micro-fabricate metallic gratings on top of the thermoelectric samples. The modified two-tint TDTR was again used to study the length-dependent thermal transport in the patterned samples. The reconstructed phonon MFP distributions for both thermoelectric samples indicate that the dominant heat-carrying phonon modes have MFPs in the a few tens to a few hundreds of nanometers range. Our measurement results on nanocrystalline $Si_{80}Ge_{20}B_{2.5}$ sample also shed light on the impact of grain boundary scattering on the microscopic distribution of phonon MFPs. The reconstructed MFP distributions provide important insight on how to further tailor the thermal conductivity of thermoelectrics to achieve higher solid-state energy conversion efficiency.

Chapter 5

Summary and Future Work

5.1 Summary

Thermal transport in non-metals is a broadband process that involves dispersive phonons with different frequencies and MFPs [44]. Understanding the distribution of heat-carrying phonon MFPs in materials has important implications for both fundamental description of microscopic energy transport and many technological applications, including thermoelectric energy conversion, thermal management in micro-/nano-electronics, and nano-enhanced photovoltaics, to name a few. In this thesis, we developed a thermal conductivity spectroscopy technique to extract the phonon MFP distributions of different materials by exploring non-diffusive thermal transport induced by grating nanostructures patterned on top of the samples of interest [14]. A heat flux suppression function based on solving the multidimensional phonon BTE is used to link the measured length-dependent thermal conductivities with the intrinsic phonon MFP distributions of the materials studied [85]. The phonon MFP distribution is reconstructed using a convex optimization algorithm [49].

Under the current algorithm framework, the heat flux suppression function for the experimental sample geometry is an essential ingredient in order to map out the phonon MFP distribution. Since the suppression function is assumed to depend only upon the sample configuration and the distribution of heat sources, we solved the gray phonon BTE across a wide range of lengthscales to find the appropriate suppression function for our sample configuration. The obtained suppression function depends upon both the characteristic heater size and the metallic pattern period. We found that both the heater size and the filling fraction significantly influence the non-diffusive thermal transport and the effective thermal conductivities have a strong dependence on which temperature we measure in the experiment [85]. When the peak temperature rise is concerned, the effective thermal conductivity decreases constantly as the heater size shrinks for a given filling fraction. The degree of non-diffusive thermal transport becomes weaker with increasing filling fraction for the same heater size, resulting in residual suppression effect for a finite filling fraction. This happens due to the transport coupling in the substrate induced by neighboring heaters. When the peak-valley temperature is considered, the dominant characteristic lengthscale becomes the gap distance between neighboring heaters. Consequently, for the same heater size, the non-diffusive transport effect is enhanced with increasing filling fraction. These results indicate the importance of accurately accounting for the temperature measurement location in the experiment.

Probing phonon MFP distribution requires the study of non-diffusive thermal transport at lengthscales comparable with phonon MFPs. Previous work utilizing localized heating are either diffraction limited by the optical wavelength or involve complex microfabrication [7]–[10], [12], [13], [15], [72]. We developed a thermal conductivity spectroscopy technique that utilizes the wire grid polarizer effect to effectively localize the heating while avoiding direct substrate heating and photo-excitation in the underlying substrate [14]. The 1D metallic patterns, with heater size down to 50 nm, were fabricated on top of the samples of interest using standard electron beam lithography. To reduce the laser light transmission into the substrate, we set up a two-tint time-domain thermoreflectance system that uses near infrared beams as both heating and probing beams [71]. The relative ~10 nm wavelength difference between pump and probe beams allows us to separate them using sharp-edge color filters. Both the pump and probe beams are linearly polarized to be parallel with the metal grating before reaching the sample surface to prevent laser transmission through the metal grating. We carried out optical simulations using COMSOL Multiphysics software package to calculate the light transmittance into the substrate and found that the transmittance is negligible for the relevant experimental lengthscales. Crystalline silicon was used as a benchmark material to demonstrate this spectroscopy technique. We fabricated metallic patterns of variable sizes on silicon and measured the light transmittance through the metal grating using a transmission measurement setup and observed that the transmittance is indeed small. We then performed thermal conductivity measurements across a range of lengthscales and temperatures and inverted the measured size-dependent thermal conductivities using the previously calculated suppression functions to reconstruct the phonon MFP distributions at different temperatures. We achieved reasonably good agreement between the reconstructed MFP distributions and the predictions from first-principle density functional theory calculations. The negligible effect of laser transmission was also confirmed by measuring the sample thermal response at different angles formed by the laser polarization and the metal grating.

We subsequently applied the phonon MFP spectroscopy technique to measure phonon MFP distributions in some select thermoelectric materials. The materials studied include $Nb_{0.95}Ti_{0.05}FeSb$ and nanocrystalline $Si_{80}Ge_{20}B_{2.5}$ samples [115]–[118], [123]. The as-received samples were prepared from powders by ball milling and hot pressing in Professor Zhifeng Ren's group at University of Houston. To improve the surface quality to be acceptable for TDTR measurement, we developed material specific recipes to polish the sample surface to achieve root-mean square roughness down to around or less than 5 nm in conjunction with a commercial polishing machine. The samples were then patterned with metallic gratings with variable line widths using electron beam lithography. We again measured the length-dependent thermal conductivities for both materials and extracted the phonon MFP distributions for both materials. We found that the dominant heat carrier MFP in $Nb_{0.95}Ti_{0.05}FeSb$ and $Si_{80}Ge_{20}B_{2.5}$ is in the tens to hundreds of nanometers range. We also observed that nanostructuring can significantly reduce the phonon MFPs below the bulk values, therefore leading to a reduced thermal conductivity. These results help gain insight into how thermal conductivity can be further tailored for next-generation of thermoelectric devices.

5.2 Future Research

Determining the heat carrier MFP distribution is of fundamental interest and also has practical implications in many energy-related applications. The state of the art phonon MFP spectroscopy technique has spatial resolution down to ~50 nm. This experimental capability allows the MFP distributions to be measurable for a wide range of materials. However, some materials of interest, such as Bi_2Te_3 and PbTe, have dominant heat-carrying phonon MFPs in the sub-100 nm range [37], [39]. To study materials with MFPs in the sub-100 nm range, future research should focus on how to further refine the spatial resolution down to ~20 nm. One option is to employ reactive ion etching (RIE) to fabricate high-quality metallic gratings down to ~20 nm to access non-diffusive thermal transport at extremely short lengthscales [98]. The major challenge here is to develop a robust microfabrication recipe. On the other hand, many current MFP spectroscopy techniques, including those indirect approaches utilizing metallic grating to access non-diffusive transport regime, involve thermal transport across a metal-substrate interface [7], [8], [10], [13], [14]. Interpreting interfacial thermal transport is typically very challenging, especially when non-diffusive thermal transport in the underlying substrate occurs simultaneously with non-equilibrium interfacial thermal transport. Future work should be expended on constructing appropriate models to address transport issues across interfaces [94].

The current convex optimization algorithm used to reconstruct the phonon MFP distribution from the measured size-dependent thermal conductivities includes a 'smoothing' parameter that balances the smoothness of the reconstructed thermal conductivity accumulation function and the accuracy of solving the thermal conductivity integral equation [49]. At present, one reasonable way of specifying an acceptable smoothing factor is to choose the minimum value that still avoids abrupt jumps in the reconstructed thermal conductivity accumulation function. Future work should try to improve the reconstruction algorithm to remove the arbitrariness of the 'smoothing' factor. For example, one may use a linear combination of some basis cumulative distribution functions to describe the thermal conductivity accumulation function and solve for the linear coefficients associated with each basis function through some optimization algorithm. Since the basis functions are already smooth, the constructed thermal conductivity accumulation function must be smooth, thus removing the smoothing factor. An alternate solution might take advantage of the shape of the differential thermal conductivity distribution function. For example, one may linearly combine some basis functions, like Gaussian probability density functions, for the differential thermal conductivity distribution function and solve for the linear coefficients through some optimization algorithm. In addition, the heat flux suppression function may depend significantly upon the sample material properties (for example, heat capacities and phonon lifetimes), particularly in the strongly non-diffusive transport regime. One exception for the previous statement is the measurement of membrane's thickness-dependent thermal conductivity in the diffusive transport regime in the TTG spectroscopy experiments, where the suppression function depends rigorously upon only the ratio of the phonon MFP to the membrane thickness [124], [125]. Generally, the dependence of the suppression function on other material properties besides the geometric ratio of phonon MFP to the characteristic thermal length makes accurate extraction of phonon MFP distributions more challenging, though [74]. Future research needs to resolve how to account for the material properties dependence of the suppression function while performing MFP reconstruction.

Bibliography

[1] G. Chen, *Nanoscale Energy Transport and Conversion.* New York: Oxford University Press, 2005.

[2] G. Chen, "Nonlocal and Nonequilibrium Heat Conduction in the Vicinity of Nanoparticles," *J. Heat Transfer*, vol. 118, no. August, pp. 539–545, 1996.

[3] P. G. Sverdrup, S. Sinha, M. Asheghi, S. Uma, and K. E. Goodson, "Measurement of ballistic phonon conduction near hotspots in silicon," *Appl. Phys. Lett.*, vol. 78, no. 21, p. 3331, 2001.

[4] R. Yang, G. Chen, M. Laroche, and Y. Taur, "Simulation of Nanoscale Multidimensional Transient Heat Conduction Problems Using Ballistic-Diffusive Equations and Phonon Boltzmann Equation," *J. Heat Transfer*, vol. 127, no. 3, pp. 298–306, 2005.

[5] S. Sinha and K. E. Goodson, "Thermal conduction in sub-100nm transistors," *Microelectronics J.*, vol. 37, no. 11, pp. 1148–1157, Nov. 2006.

[6] Y. Koh and D. Cahill, "Frequency dependence of the thermal conductivity of semiconductor alloys," *Phys. Rev. B*, vol. 76, no. 7, p. 075207, Aug. 2007.

[7] M. E. Siemens, Q. Li, R. Yang, K. A. Nelson, E. H. Anderson, M. M. Murnane, and H. C. Kapteyn, "Quasi-ballistic thermal transport from nanoscale interfaces observed using ultrafast coherent soft X-ray beams.," *Nat. Mater.*, vol. 9, no. 1, pp. 26–30, Jan. 2010.

[8] A. J. Minnich, J. A. Johnson, A. J. Schmidt, K. Esfarjani, M. S. Dresselhaus, K. A. Nelson, and G. Chen, "Thermal Conductivity Spectroscopy Technique to Measure Phonon Mean Free Paths," *Phys. Rev. Lett.*, vol. 107, no. 9, p. 095901, Aug. 2011.

[9] J. A. Johnson, A. A. Maznev, J. Cuffe, J. K. Eliason, A. J. Minnich, T. Kehoe, C. M. S. Torres, G. Chen, and K. A. Nelson, "Direct Measurement of Room-Temperature Nondiffusive Thermal Transport Over Micron Distances in a Silicon Membrane,"

Phys. Rev. Lett., vol. 110, no. 2, p. 025901, Jan. 2013.

[10] K. T. Regner, D. P. Sellan, Z. Su, C. H. Amon, A. J. H. McGaughey, and J. A. Malen, "Broadband phonon mean free path contributions to thermal conductivity measured using frequency domain thermoreflectance.," *Nat. Commun.*, vol. 4, p. 1640, Jan. 2013.

[11] K. C. Collins, A. A. Maznev, J. Cuffe, K. A. Nelson, and G. Chen, "Examining thermal transport through a frequency-domain representation of time-domain thermoreflectance data," *Rev. Sci. Instrum.*, vol. 85, no. 12, p. 124903, Dec. 2014.

[12] K. M. Hoogeboom-Pot, J. N. Hernandez-Charpak, X. Gu, T. D. Frazer, E. H. Anderson, W. Chao, R. W. Falcone, R. Yang, M. M. Murnane, H. C. Kapteyn, and D. Nardi, "A new regime of nanoscale thermal transport: Collective diffusion increases dissipation efficiency," *Proc. Natl. Acad. Sci.*, vol. 112, no. 16, pp. 4846–4851, Mar. 2015.

[13] Y. Hu, L. Zeng, A. J. Minnich, M. S. Dresselhaus, and G. Chen, "Spectral Mapping of Thermal Conductivity through Nanoscale Ballistic Transport," *Nat. Nanotechnol.*, vol. 10, pp. 701–706, 2015.

[14] L. Zeng, K. C. Collins, Y. Hu, M. N. Luckyanova, A. A. Maznev, S. Huberman, V. Chiloyan, J. Zhou, X. Huang, K. A. Nelson, and G. Chen, "Measuring phonon mean free path distributions by probing quasiballistic phonon transport in grating nanostructures," *Sci. Rep.*, vol. 5, p. 17131, 2015.

[15] J. Cuffe, J. K. Eliason, A. A. Maznev, K. C. Collins, J. A. Johnson, A. Shchepetov, M. Prunnila, J. Ahopelto, C. M. Sotomayor Torres, G. Chen, and K. A. Nelson, "Reconstructing phonon mean-free-path contributions to thermal conductivity using nanoscale membranes," *Phys. Rev. B*, vol. 91, no. 24, p. 245423, Jun. 2015.

[16] D. G. Cahill, W. K. Ford, K. E. Goodson, G. D. Mahan, A. Majumdar, H. J. Maris, R. Merlin, and S. R. Phillpot, "Nanoscale thermal transport," *J. Appl. Phys.*, vol. 93, no. 2, p. 793, 2003.

[17] M. N. Luckyanova, J. Garg, K. Esfarjani, A. Jandl, M. T. Bulsara, A. J. Schmidt, A. J. Minnich, S. Chen, M. S. Dresselhaus, Z. Ren, E. A. Fitzgerald, and G. Chen, "Coherent Phonon Heat Conduction in Superlattices," *Science*, vol. 2360, no. 2009, 2012.

[18] A. M. Marconnet and K. E. Goodson, "From the Casimir Limit to Phononic Crystals:

20 Years of Phonon Transport Studies Using Silicon-on-Insulator Technology," *J. Heat Transfer*, vol. 135, no. 6, p. 061601, 2013.

[19] A. M. Marconnet, M. A. Panzer, and K. E. Goodson, "Thermal conduction phenomena in carbon nanotubes and related nanostructured materials," *Rev. Mod. Phys.*, vol. 85, no. 3, pp. 1295–1326, Aug. 2013.

[20] D. G. Cahill, P. V. Braun, G. Chen, D. R. Clarke, S. Fan, K. E. Goodson, P. Keblinski, W. P. King, G. D. Mahan, A. Majumdar, H. J. Maris, S. R. Phillpot, E. Pop, and L. Shi, "Nanoscale thermal transport. II. 2003–2012," *Appl. Phys. Rev.*, vol. 1, no. 1, p. 011305, Mar. 2014.

[21] M. N. Luckyanova, J. Mendoza, H. Lu, S. Huang, J. Zhou, M. Li, B. J. Kirby, A. J. Grutter, A. A. Puretzky, M. S. Dresselhaus, A. Gossard, and G. Chen, "Phonon Localization in Heat Conduction," *arXiv Prepr. arXiv*, pp. 1–28, 2016.

[22] R. Venkatasubramanian, E. Siivola, T. Colpitts, and B. O'Quinn, "Thin-film thermoelectric devices with high room-temperature figures of merit.," *Nature*, vol. 413, no. 6856, pp. 597–602, Oct. 2001.

[23] J. Yang, "Potential applications of thermoelectric waste heat recovery in the automotive industry," *ICT 2005. 24th Int. Conf. Thermoelectr. 2005.*, pp. 170–174, 2005.

[24] M. S. Dresselhaus, G. Chen, M. Y. Tang, R. G. Yang, H. Lee, D. Z. Wang, Z. F. Ren, J.-P. Fleurial, and P. Gogna, "New Directions for Low-Dimensional Thermoelectric Materials," *Adv. Mater.*, vol. 19, no. 8, pp. 1043–1053, Apr. 2007.

[25] B. Poudel, Q. Hao, Y. Ma, Y. Lan, A. Minnich, B. Yu, X. Yan, D. Wang, A. Muto, D. Vashaee, X. Chen, J. Liu, M. S. Dresselhaus, G. Chen, and Z. Ren, "High-thermoelectric performance of nanostructured bismuth antimony telluride bulk alloys.," *Science*, vol. 320, no. 5876, pp. 634–638, May 2008.

[26] A. I. Hochbaum, R. Chen, R. D. Delgado, W. Liang, E. C. Garnett, M. Najarian, A. Majumdar, and P. Yang, "Enhanced thermoelectric performance of rough silicon nanowires.," *Nature*, vol. 451, no. 7175, pp. 163–167, Jan. 2008.

[27] A. I. Boukai, Y. Bunimovich, J. Tahir-Kheli, J.-K. Yu, W. a Goddard, and J. R. Heath, "Silicon nanowires as efficient thermoelectric materials.," *Nature*, vol. 451, no. 7175, pp. 168–171, Jan. 2008.

[28] A. J. Minnich, M. S. Dresselhaus, Z. F. Ren, and G. Chen, "Bulk nanostructured thermoelectric materials: current research and future prospects," *Energy Environ. Sci.*, vol. 2, no. 5, pp. 466–479, 2009.

[29] J.-K. Yu, S. Mitrovic, D. Tham, J. Varghese, and J. R. Heath, "Reduction of thermal conductivity in phononic nanomesh structures.," *Nat. Nanotechnol.*, vol. 5, no. 10, pp. 718–721, Oct. 2010.

[30] G. Pernot, M. Stoffel, I. Savic, F. Pezzoli, P. Chen, G. Savelli, a Jacquot, J. Schumann, U. Denker, I. Mönch, C. Deneke, O. G. Schmidt, J. M. Rampnoux, S. Wang, M. Plissonnier, a Rastelli, S. Dilhaire, and N. Mingo, "Precise control of thermal conductivity at the nanoscale through individual phonon-scattering barriers.," *Nat. Mater.*, vol. 9, no. 6, pp. 491–5, Jun. 2010.

[31] M. Zebarjadi, K. Esfarjani, M. S. Dresselhaus, Z. F. Ren, and G. Chen, "Perspectives on thermoelectrics: from fundamentals to device applications," *Energy Environ. Sci.*, vol. 5, no. 1, p. 5147, 2012.

[32] J. P. Freedman, J. H. Leach, E. A. Preble, Z. Sitar, R. F. Davis, and J. A. Malen, "Universal phonon mean free path spectra in crystalline semiconductors at high temperatur," *Sci. Rep.*, vol. 3, p. 2963, Jan. 2013.

[33] A. J. Minnich, "Advances in the measurement and computation of thermal phonon transport properties," *J. Phys. Condens. Matter*, vol. 27, no. 5, p. 053202, Mar. 2015.

[34] K. T. Regner, J. P. Freedman, and J. A. Malen, "Advances in Studying Phonon Mean-Free-Path-Dependent Contributions to Thermal Conductivity," *Nanoscale Microscale Thermophys. Eng.*, vol. 19, no. 3, pp. 183–205, 2015.

[35] A. Ward and D. A. Broido, "Intrinsic phonon relaxation times from first-principles studies of the thermal conductivities of Si and Ge," *Phys. Rev. B*, vol. 81, no. 8, p. 085205, Feb. 2010.

[36] K. Esfarjani, G. Chen, and H. T. Stokes, "Heat transport in silicon from first-principles calculations," *Phys. Rev. B*, vol. 84, no. 8, p. 085204, Aug. 2011.

[37] Z. Tian, J. Garg, K. Esfarjani, T. Shiga, J. Shiomi, and G. Chen, "Phonon conduction in PbSe, PbTe, and PbTe_{1−x}Se_{x} from first-principles calculations," *Phys. Rev. B*, vol. 85, no. 18, p. 184303, May 2012.

[38] L. Lindsay, D. a. Broido, and T. L. Reinecke, "First-Principles Determination of

Ultrahigh Thermal Conductivity of Boron Arsenide: A Competitor for Diamond?," *Phys. Rev. Lett.*, vol. 111, no. 2, p. 025901, Jul. 2013.

[39] O. Hellman and D. A. Broido, "Phonon thermal transport in Bi2Te3 from first principles," *Phys. Rev. B*, vol. 90, no. 13, p. 134309, Oct. 2014.

[40] C. Dames and G. Chen, "Thermal Conductivity of Nanostructured Thermoelectric Materials," *Thermoelectr. Handb. Macro to Nano*, no. 42, pp. 1–16, 2006.

[41] J. Callaway, "Model for lattice thermal conductivity at low temperatures," *Phys. Rev.*, vol. 113, no. 4, p. 1046, 1959.

[42] M. Holland, "Analysis of Lattice Thermal Conductivity," *Phys. Rev.*, vol. 132, no. 6, pp. 2461–2471, Dec. 1963.

[43] K. Esfarjani, J. Garg, and G. Chen, "Modeling Heat Conduction From First-Principles," *Annu. Rev. Heat Transf.*, vol. 17, pp. 9–47, 2014.

[44] Z. Tian, S. Lee, and G. Chen, "Heat Transfer in Thermoelectric Materials and Devices," *J. Heat Transfer*, vol. 135, no. 6, p. 061605, May 2013.

[45] O. Delaire, J. Ma, K. Marty, A. F. May, M. A. McGuire, M.-H. Du, D. J. Singh, A. Podlesnyak, G. Ehlers, M. D. Lumsden, and B. C. Sales, "Giant anharmonic phonon scattering in PbTe.," *Nat. Mater.*, vol. 10, no. 8, pp. 614–9, Aug. 2011.

[46] J. Ma, O. Delaire, A. F. May, C. E. Carlton, M. A. McGuire, L. H. VanBebber, D. L. Abernathy, G. Ehlers, T. Hong, A. Huq, W. Tian, V. M. Keppens, Y. Shao-Horn, and B. C. Sales, "Glass-like phonon scattering from a spontaneous nanostructure in AgSbTe2.," *Nat. Nanotechnol.*, vol. 8, no. 6, pp. 445–51, Jun. 2013.

[47] A. J. Minnich, "Exploring Electron and Phonon Transport at the Nanoscale for Thermoelectric Energy Conversion," Massachusetts Institute of Technology, 2011.

[48] A. . Maznev, J. A. Johnson, and K. A. Nelson, "Onset of nondiffusive phonon transport in transient thermal grating decay," *Phys. Rev. B*, vol. 84, no. 19, p. 195206, Nov. 2011.

[49] A. J. Minnich, "Determining phonon mean free paths from observations of quasiballistic thermal transport.," *Phys. Rev. Lett.*, vol. 109, no. 20, p. 205901, Nov. 2012.

[50] D. G. Cahill, "Analysis of heat flow in layered structures for time-domain thermoreflectance," *Rev. Sci. Instrum.*, vol. 75, no. 12, p. 5119, 2004.

[51] A. J. Schmidt, X. Chen, and G. Chen, "Pulse accumulation, radial heat conduction, and anisotropic thermal conductivity in pump-probe transient thermoreflectance," *Rev. Sci. Instrum.*, vol. 79, no. 11, p. 114902, Nov. 2008.

[52] M. Grant and S. Boyd, *Graph implementations for nonsmooth convex programs, Recent Advances in Learning and Control (a tribute to M. Vidyasagar), V. Blondel, S. Boyd, and H. Kimura, editors, pages 95-110, Lecture Notes in Control and Information Sciences*. Springer, 2008.

[53] M. Grant and S. Boyd, *CVX: Matlab software for disciplined convex programming, version 2.0 beta. http://cvxr.com/cvx.* .

[54] K. C. Collins, A. A. Maznev, Z. Tian, K. Esfarjani, K. A. Nelson, and G. Chen, "Non-diffusive relaxation of a transient thermal grating analyzed with the Boltzmann transport equation," *J. Appl. Phys.*, vol. 114, p. 104302, 2013.

[55] C. Hua and A. J. Minnich, "Semi-analytical solution to the frequency-dependent Boltzmann transport equation for cross-plane heat conduction in thin films," *J. Appl. Phys.*, vol. 117, no. 17, p. 175306, May 2015.

[56] C. A. Paddock and G. L. Eesley, "Transient thermoreflectance from thin metal films," *J. Appl. Phys.*, vol. 60, no. 1, pp. 285 – 290, 1986.

[57] W. S. Capinski, H. J. Maris, W. S. Capinski, and H. J. Maris, "Improved apparatus for picosecond pump-and-probe optical measurements Improved apparatus for picosecond pump-and-probe optical measurements," *J. Appl. Phys.*, vol. 67, no. 8, pp. 2720 – 2726, 1996.

[58] D. G. Cahill, K. Goodson, and A. Majumdar, "Thermometry and Thermal Transport in Micro/Nanoscale Solid-State Devices and Structures," *J. Heat Transfer*, vol. 124, no. 2, p. 223, 2002.

[59] A. J. Schmidt, "Pump-Probe Thermoreflectance," *Annu. Rev. Heat Transf.*, vol. 16, no. 1, pp. 159–181, 2013.

[60] T. Q. Qiu and C. L. Tien, "Short-pulse laser heating on metals," *Int. J. Heat Mass Transf.*, vol. 35, no. 3, pp. 719–726, 1992.

[61] T. Q. Qiu and C. L. Tien, "Heat Transfer Mechanisms During Short-Pulse Laser Heating of Metals," *J. Heat Transfer*, vol. 115, no. November 1993, pp. 835–841, 1993.

[62] T. Q. Qiu and C. L. Tien, "Femtosecond laser heating of multi-layer," *Int. J. Heat Mass Transf.*, vol. 37, no. 17, pp. 2789–2797, 1994.

[63] T. Q. Qiu, T. Juhasz, C. Suarez, and W. E. Brons, "Femtosecond laser heating of multi-layer metals - II. Experiments," *Int. J. Heat Mass Transf.*, vol. 37, no. 17, pp. 2799–2808, 1994.

[64] S. D. Broson, J. G. Fujimoto, and E. P. Ippen, "Femtosecond Electronic Heat-Transport Dynamics in Thin Gold Films," *Phys. Rev. Lett.*, vol. 59, no. 17, pp. 1962–1965, 1987.

[65] R. W. Schoenlein, W. Z. Lin, J. G. Fujimoto, and G. L. Eesley, "Femtosecond studies of nonequilibrium electronic processes in metals," *Phys. Rev. Lett.*, vol. 58, no. 16, pp. 1680–1683, 1987.

[66] W. S. Fann, R. Storz, and W. K. Tom, "Electron thermalization in gold," *Phys. Rev. B*, vol. 46, no. 20, pp. 13592–13595, 1992.

[67] A. Majumdar and P. Reddy, "Role of electron–phonon coupling in thermal conductance of metal–nonmetal interfaces," *Appl. Phys. Lett.*, vol. 84, no. 23, p. 4768, 2004.

[68] A. J. Schmidt, "Optical Characterization of Thermal Transport from the Nanoscale to the Macroscale," Massachusetts Institute of Technology, 2008.

[69] H. Carslaw and J. Jaeger, *Conduction of Heat in Solids*. Oxford University Press, 1959.

[70] E. Swartz and R. Pohl, "Thermal boundary resistance," *Rev. Mod. Phys.*, vol. 61, no. 3, pp. 605–668, Jul. 1989.

[71] K. Kang, Y. K. Koh, C. Chiritescu, X. Zheng, and D. G. Cahill, "Two-tint pump-probe measurements using a femtosecond laser oscillator and sharp-edged optical filters.," *Rev. Sci. Instrum.*, vol. 79, no. 11, p. 114901, Nov. 2008.

[72] J. A. Johnson, J. K. Eliason, A. A. Maznev, T. Luo, and K. A. Nelson, "Non-diffusive thermal transport in GaAs at micron length scales," *J. Appl. Phys.*, vol. 118, no. 15, p.

155104, Oct. 2015.

[73] L. Zeng, V. Chiloyan, S. Huberman, A. A. Maznev, J. M. Peraud, G. Nicolas, K. A. Nelson, and G. Chen, "Monte Carlo study of non-diffusive relaxation of a transient thermal grating in thin membranes Monte Carlo study of non-diffusive relaxation of a transient thermal grating in thin membranes," *Appl. Phys. Lett.*, vol. 108, p. 063107, 2016.

[74] V. Chiloyan, L. Zeng, S. Huberman, A. A. Maznev, K. A. Nelson, and G. Chen, "A Variational Approach to Extracting the Phonon Mean Free Path Distribution from the Spectral Boltzmann Transport Equation," *arXiv Prepr. arXiv*, vol. 1511.08989, 2015.

[75] A. Majumdar, "Microscale Heat Conduction in Dielectric Thin Films," *J. Heat Transfer*, vol. 115, no. February, pp. 7–16, 1993.

[76] A. A. Joshi and A. Majumdar, "Transient ballistic and diffusive phonon heat transport in thin films," *J. Appl. Phys.*, vol. 74, no. 1, pp. 31–39, 1993.

[77] S. V. J. Narumanchi, J. Y. Murthy, and C. H. Amon, "Submicron Heat Transport Model in Silicon Accounting for Phonon Dispersion and Polarization," *J. Heat Transfer*, vol. 126, no. 6, p. 946, 2004.

[78] G. Chen, "Size and Interface Effects on Thermal Conductivity of Superlattices and Periodic Thin-Film Structures," *J. Heat Transfer*, vol. 119, no. 2, p. 220, 1997.

[79] G. Chen, "Thermal conductivity and ballistic-phonon transport in the cross-plane direction of superlattices," *Phys. Rev. B*, vol. 57, no. 23, pp. 14958–14973, Jun. 1998.

[80] G. Chen and T. Zeng, "NONEQUILIBRIUM PHONON AND ELECTRON TRANSPORT IN HETEROSTRUCTURES AND SUPERLATTICES," *Microscale Thermophys. Eng.*, vol. 5, pp. 71–88, 2001.

[81] G. Chen, "Ballistic-Diffusive Heat-Conduction Equations," *Phys. Rev. Lett.*, vol. 86, no. 11, pp. 2297–2300, Mar. 2001.

[82] S. V. J. Narumanchi, J. Y. Murthy, and C. H. Amon, "Simulation of Unsteady Small Heat Source Effects in Sub-Micron Heat Conduction," *J. Heat Transfer*, vol. 125, no. 5, p. 896, 2003.

[83] J. Y. Murthy and S. R. Mathur, "An Improved Computational Procedure for Sub-Micron Heat Conduction," *J. Heat Transfer*, vol. 125, no. 5, p. 904, 2003.

[84] A. J. Minnich, G. Chen, S. Mansoor, and B. S. Yilbas, "Quasiballistic heat transfer studied using the frequency-dependent Boltzmann transport equation," *Phys. Rev. B*, vol. 84, no. 23, p. 235207, Dec. 2011.

[85] L. Zeng and G. Chen, "Disparate quasiballistic heat conduction regimes from periodic heat sources on a substrate," *J. Appl. Phys.*, vol. 116, no. 6, p. 064307, Aug. 2014.

[86] Q. Hao, G. Chen, and M.-S. Jeng, "Frequency-dependent Monte Carlo simulations of phonon transport in two-dimensional porous silicon with aligned pores," *J. Appl. Phys.*, vol. 106, no. 11, p. 114321, 2009.

[87] J.-P. M. Péraud, "Low Variance Methods for Monte Carlo Simulation of Phonon Transport," Massachusetts Institute of Technology, 2011.

[88] J.-P. M. Péraud and N. G. Hadjiconstantinou, "Efficient simulation of multidimensional phonon transport using energy-based variance-reduced Monte Carlo formulations," *Phys. Rev. B*, vol. 84, no. 20, p. 205331, Nov. 2011.

[89] J.-P. M. Péraud and N. G. Hadjiconstantinou, "An alternative approach to efficient simulation of micro/nanoscale phonon transport," *Appl. Phys. Lett.*, vol. 101, no. 15, p. 153114, 2012.

[90] J.-P. M. Péraud, C. D. Landon, and N. G. Hadjiconstantinou, "Monte Carlo Methods for Solving the Boltzmann Transport Equation," *Annu. Rev. Heat Transf.*, vol. 17, pp. 205–265, 2014.

[91] L. J. Challis, "Kapitza resistance and acoustic transmission across boundaries at high frequencies," *J. Phys. C Solid State Phys.*, vol. 7, pp. 481–495, 1974.

[92] E. T. Swartz and R. O. Pohl, "Thermal resistance at interfaces," *Appl. Phys. Lett.*, vol. 51, no. 26, p. 2200, 1987.

[93] P. Reddy, K. Castelino, and A. Majumdar, "Diffuse mismatch model of thermal boundary conductance using exact phonon dispersion," *Appl. Phys. Lett.*, vol. 87, no. 21, p. 211908, 2005.

[94] C. Hua, X. Chen, K. Ravichandran, and A. J. Minnich, "Fresnel transmission coefficients for thermal phonons at solid interfaces," *arXiv Prepr. arXiv*, pp. 1–24, 2015.

[95] Y. Chalopin, J.-N. Gillet, and S. Volz, "Predominance of thermal contact resistance in a silicon nanowire on a planar substrate," *Phys. Rev. B*, vol. 77, no. 23, p. 233309, Jun. 2008.

[96] R. B. Wilson, J. P. Feser, G. T. Hohensee, and D. G. Cahill, "Two-channel model for nonequilibrium thermal transport in pump-probe experiments," *Phys. Rev. B*, vol. 88, no. 14, p. 144305, Oct. 2013.

[97] Z. Tian, S. Lee, and G. Chen, "Heat Transfer in Thermoelectric Materials and Devices," *J. Heat Transfer*, vol. 135, no. 6, p. 061605, 2013.

[98] K. C. Collins, "Studies of non-diffusive heat conduction through spatially periodic and time-harmonic thermal excitations," Massachusetts Institute of Technology, 2015.

[99] COMSOL, *Wave Optics Module Model Library Manual*. 2013.

[100] T. W. Ebbesen, H. J. Lezec, H. F. Ghaemi, T. Thio, and P. A. Wolff, "Extraordinary optical transmission through sub-wavelength hole arrays," *Nature*, vol. 391, no. February, pp. 667–669, 1998.

[101] E. Hecht, *Optics*, 4th ed. Addison Wesley, 2002.

[102] J. J. Wang, L. Chen, X. Liu, P. Sciortino, F. Liu, F. Walters, and X. Deng, "30-nm-wide aluminum nanowire grid for ultrahigh contrast and transmittance polarizers made by UV-nanoimprint lithography," *Appl. Phys. Lett.*, vol. 89, no. 14, p. 141105, 2006.

[103] R. B. Wilson and D. G. Cahill, "Anisotropic failure of Fourier theory in time-domain thermoreflectance experiments.," *Nat. Commun.*, vol. 5, p. 5075, Jan. 2014.

[104] A. V. Inyushkin, A. N. Taldenkov, A. M. Gibin, A. V. Gusev, and H.-J. Pohl, "On the isotope effect in thermal conductivity of silicon," *Phys. Status Solidi*, vol. 1, no. 11, pp. 2995–2998, Nov. 2004.

[105] C. J. Glassbrenner and G. A. Slack, "Thermal Conductivity of Silicon and Germanium from 3K to the Melting Point," *Phys. Rev.*, vol. 134, p. A1058, 1964.

[106] D. Ding, X. Chen, and A. J. Minnich, "Radial quasiballistic transport in time-domain thermoreflectance studied using Monte Carlo simulations," *Appl. Phys. Lett.*, vol. 104, no. 14, p. 143104, Apr. 2014.

[107] J. Zhou, B. Liao, B. Qiu, S. Huberman, K. Esfarjani, M. S. Dresselhaus, and G. Chen, "Ab initio optimization of phonon drag effect for lower-temperature thermoelectric energy conversion," *Proc. Natl. Acad. Sci.*, vol. 112, no. 48, pp. 14777–14782, 2015.

[108] N. W. Ashcroft and N. D. Mermin, *Solid State Physics*. Saunders College Publishers, Fort Worth, TX, 1976.

[109] M. Lundstrom, *Fundamentals of Carrier Transport*. Cambridge University Press, 2000.

[110] L. D. Hicks, T. C. Harman, and M. S. Dresselhaus, "Use of quantum-well superlattices to obtain a high figure of merit from nonconventional thermoelectric materials," *Appl. Phys. Lett.*, vol. 63, no. 23, p. 3230, 1993.

[111] L. Hicks, T. Harman, X. Sun, and M. Dresselhaus, "Experimental study of the effect of quantum-well structures on the thermoelectric figure of merit.," *Phys. Rev. B. Condens. Matter*, vol. 53, no. 16, pp. R10493–R10496, Apr. 1996.

[112] K. Biswas, J. He, I. D. Blum, C.-I. Wu, T. P. Hogan, D. N. Seidman, V. P. Dravid, and M. G. Kanatzidis, "High-performance bulk thermoelectrics with all-scale hierarchical architectures.," *Nature*, vol. 489, no. 7416, pp. 414–8, Sep. 2012.

[113] A. Minnich and G. Chen, "Modified effective medium formulation for the thermal conductivity of nanocomposites," *Appl. Phys. Lett.*, vol. 91, p. 073105, 2007.

[114] H. Zhang and A. J. Minnich, "The best nanoparticle size distribution for minimum thermal conductivity," *Sci. Rep.*, vol. 5, p. 8995, 2015.

[115] G. Joshi, R. He, M. Engber, G. Samsonidze, T. Pantha, E. Dahal, K. Dahal, J. Yang, Y. Lan, B. Kozinsky, and Z. Ren, "NbFeSb-based p-type half-Heusler for power generation applications," *Energy Environ. Sci.*, vol. 7, pp. 4070–4076, 2014.

[116] G. Joshi, H. Lee, Y. Lan, X. Wang, G. Zhu, D. Wang, R. W. Gould, D. C. Cuff, M. Y. Tang, M. S. Dresselhaus, G. Chen, and Z. Ren, "Enhanced Thermoelectric Figure-of-Merit in Nanostructured p-type Silicon Germanium Bulk Alloys," *Nano Lett.*, vol. 8, no. 12, pp. 4670–4674, 2008.

[117] X. W. Wang, H. Lee, Y. C. Lan, G. H. Zhu, G. Joshi, D. Z. Wang, J. Yang, A. J. Muto, M. Y. Tang, J. Klatsky, S. Song, M. S. Dresselhaus, and G. Chen, "Enhanced thermoelectric figure of merit in nanostructured n -type silicon germanium bulk alloy," *Appl. Phys. Lett.*, vol. 93, p. 193121, 2008.

[118] G. H. Zhu, H. Lee, Y. C. Lan, X. W. Wang, G. Joshi, D. Z. Wang, J. Yang, D. Vashaee, H. Guilbert, A. Pillitteri, M. S. Dresselhaus, G. Chen, and Z. F. Ren, "Increased Phonon Scattering by Nanograins and Point Defects in Nanostructured Silicon with a Low Concentration of Germanium," *Phys. Rev. Lett.*, vol. 102, p. 196803, 2009.

[119] R. He, D. Kraemer, J. Mao, L. Zeng, Q. Jie, Y. Lan, C. Li, J. Shuai, H. S. Kim, Y. Liu, D. Broido, G. Chen, and Z. Ren, "Achieving high power factor and output power density in p-type half-Heuslers Nb1-xTixFeSb," p. In review, 2016.

[120] H. Feng, B. Yu, S. Chen, K. Collins, C. He, Z. Ren, and G. Chen, "Studies on surface preparation and smoothness of nanostructured Bi2Te3-based alloys by electrochemical and mechanical methods," *Electrochim. Acta*, vol. 56, no. 8, pp. 3079–3084, 2010.

[121] K. Ga, S. Populoh, L. Sagarna, L. Karvonen, W. Xie, A. Beni, P. Schmutz, and A. Weidenkaff, "Phase formation, stability, and oxidation in (Ti, Zr, Hf)NiSn half-Heusler compounds," *Phys. Status Solidi A*, vol. 211, no. 6, pp. 1259–1266, 2014.

[122] J. Garg, N. Bonini, B. Kozinsky, and N. Marzari, "Role of Disorder and Anharmonicity in the Thermal Conductivity of Silicon-Germanium Alloys: A First-Principles Study," *Phys. Rev. Lett.*, vol. 106, no. 4, p. 045901, Jan. 2011.

[123] Z. Wang, J. E. Alaniz, W. Jang, J. E. Garay, and C. Dames, "Thermal Conductivity of Nanocrystalline Silicon : Importance of Grain Size and Frequency-Dependent Mean Free Paths," *Nano Lett.*, vol. 11, no. 6, pp. 2206–2213, 2011.

[124] K. Fuchs and N. F. Mott, "The conductivity of thin metallic films according to the electron theory of metals," *Math. Proc. Cambridge Philos. Soc.*, vol. 34, no. 01, p. 100, Oct. 1938.

[125] E. H. Sondheimer, *The Mean Free Path of Electrons in Metals*. Taylor and Francis, Oxford, 1952.